Revision 2 for Manuscript 7812

Incorporation mechanism of structurally bound gold in pyrite: Insights from an integrated chemical and atomic-scale microstructural study

Lei Meng[1,2], Sanyuan Zhu[3], Xiaochun Li[4], Wei Terry Chen[5], Haiyang Xian[1], Xinyu Gao[6], Taiping Zhao[1,2,*]

[1]Key Laboratory of Mineralogy and Metallogeny, Guangzhou Institute of Geochemistry, Chinese Academy of Sciences, Guangzhou 510640, China

[2]CAS Center for Excellence in Deep Earth Science, Guangzhou 510640, China

[3]State Key Laboratory of Organic Geochemistry, Guangzhou Institute of Geochemistry, Chinese Academy of Sciences, Guangzhou 510640, China

[4]Key Laboratory of Mineral Resources, Institute of Geology and Geophysics, Chinese Academy of Sciences, Beijing 100029, China

[5]State Key Laboratory of Ore Deposit Geochemistry, Institute of Geochemistry, Chinese Academy of Sciences, Guiyang 550002, China

[6] Guangdong Polytechnic of Water Resources and Electric Engineering, Guangzhou 510635, China

[*]Corresponding author Address: 511 Kehua Street, Wushan, Tianhe District, Guangzhou, GD 510640; E-mail: **tpzhao@gig.ac.cn**; Tel.:+86 20 85290231

Abstract

Pyrite is one of the most important carriers for Au in hydrothermal deposits, but the incorporation mechanism of structurally bound Au has long been a matter of

debate due to poor understanding of chemical state and atomic-scale structure of Au in the pyrite lattice. Arsenian pyrite is the dominant Au-hosting mineral from the Shanggong Au deposit (130t Au) in the southern margin of the North China Craton. New EPMA and LA-ICP-MS results show that the arsenian pyrite has remarkably high Au (0.05-0.78 wt%) and As (0.39-4.60 wt%). Au is negatively correlated with Fe but positively correlated with As. Z-contrast HAADF-STEM imaging reveals that Au atoms sit at the Fe atom sites in the lattice of the arsenian pyrite. Our μ-XANES results and previously reported data suggest that Au and As in arsenian pyrite are predominant of chemically bound Au^{+} and As^{-}, respectively. We thus propose that Au^{+} and As^{-} are both structurally bound and sit at the Fe and S atom sites of pyrite, respectively. As may not be necessary but favorable for the incorporation of structurally bound Au in pyrite. Our study has significant implications for understanding the enrichment mechanism of Au from ore-forming fluids with low Au and As concentrations into arsenian pyrite and for exploring the role of As in Au mineralization of hydrothermal deposits.

Keywords: arsenian pyrite, μ-XANES spectroscopy, Z-contrast HAADF-STEM image, Au incorporation mechanism

Introduction

Pyrite, the most common sulfide in the Earth's crust, has long been considered to be economically significant because it hosts large amounts of Au and many other trace elements, such as As, Tl, Te, Sb, and Se (Reich et al. 2005; Deditius et al. 2014). A positive correlation between Au and As in pyrite has been well recognized and is

taken to indicate the control of As on Au enrichment (Reich et al. 2005; Deditius et al. 2014; Kusebauch et al. 2019; Xing et al. 2019). Arsenian pyrite is also a common mineral in hydrothermal ore deposits such as Carlin, epithermal, and orogenic Au deposits (Fleet and Mumin 1997; Cline 2001; Reich et al. 2005; Deditius et al. 2014 and references therein). Invisible Au accounts for the majority of Au in arsenian pyrite, and occurs as structurally bound Au and/or Au-bearing nanoparticles (Reich et al. 2005; Deditius et al. 2014; Filimonova et al. 2020 and references therein). Although the incorporation mechanism of structurally bound Au in arsenian pyrite has been extensively investigated (Arehart et al. 1993; Fleet and Mumin 1997; Simon et al. 1999a, 1999b; Palenik et al. 2004; Chouinard et al. 2005; Reich et al. 2005; Deditius et al. 2008), it remains a matter of debate. Precise chemical state and atomic-scale structural features of Au in the pyrite lattice are still poorly understood.

The state of Au in pyrite has attracted many studies in the past three decades (Arehart et al. 1993; Simon et al. 1999a; Palenik et al. 2004; Deditius et al. 2008; and references therein), but is still not absolutely convincing confirmed. It was traditionally considered that structurally bound Au is likely present as Au^{+} (Simon et al. 1999a; Reich et al. 2005; Deditius et al. 2014) or Au^{3+} (Arehart et al. 1993; Chouinard et al. 2005) in the lattice of arsenian pyrite, but Au^{3+} has not been confirmed by spectroscopic data. Au^{0} and ionic Au^{+} in Au-bearing arsenian pyrite were identified by X-ray absorption near edge structure spectroscopy (XANES) with a broad-beam of 15×1 mm (Simon et al. 1999a). However, the broad beam can potentially produce mixed spectra of different states of Au. In addition, the coupled

66 occurrence of Au and As makes it more difficult to identify the exact chemical state
67 and local structure of Au in arsenian pyrite because Au XANES spectra can be partly
68 obscured by that of As (Merkulova et al. 2019). Such issues were further addressed by
69 using recently developed high energy-resolution X-ray absorption spectroscopy
70 (HERFD-XAS) (Trigub et al. 2017; Merkulova et al. 2019; Pokrovski et al. 2019;
71 Filimonova et al., 2020). Trigub et al. (2017) reported that chemically bound Au
72 replaces Fe in the synthesized As-free hydrothermal pyrite structure. Inversely,
73 Pokrovski et al. (2019) proposed that chemically bound Au^{+} in As-poor pyrite mainly
74 occurs in Au_2S clusters. Merkulova et al. (2019) reported that chemically bound Au^{+}
75 also replaces Fe^{2+} in the arsenian pyrite structure. Filimonova et al. (2020)
76 demonstrated that chemically bound Au^{+} in As-free and/or arsenian pyrite is present
77 as both structural Au^{+} that substitutes for Fe^{2+} in the pyrite lattice and Au_2S-like
78 inclusions. Given these results, understanding of the chemical state of structurally
79 bound Au in pyrite remains elusive due to the diversity of natural samples (depending
80 on the deposit type and ore formation conditions), low concentrations and
81 heterogeneous distribution of Au in arsenian pyrite, and even controversial
82 interpretations of the XAS results (Cabri et al. 2000; Pokrovski et al. 2014;
83 Filimonova et al. 2020).

84 In this study, we investigated the *in-situ* chemical and textural features of pyrite
85 from the Shanggong Au deposit in the southern margin of the North China Craton by
86 using high-resolution spectroscopic techniques. The Shanggong deposit is an epizonal
87 orogenic Au deposit, containing 130t Au at an average ore grade of 2-7g/t (No.1

Institute of Geological & Mineral Resource Survey of Henan, China, report, 2019). Arsenian pyrite is the foremost Au carrier in the deposit. Chemical compositions of Au-rich arsenian pyrite were obtained by using electron probe microanalysis (EPMA), and laser ablation-inductively coupled plasma-mass spectrometry (LA-ICP-MS). Atomic-scale microstructural data were obtained by aberration-corrected scanning transmission electron microscopy (ACSTEM). Furthermore, *in-situ* micro-X-ray absorption near edge structure (μ-XANES) was utilized to determine the chemical speciation of Au and As in the arsenian pyrite. The new dataset allows us to comprehensively constrain the chemical state and incorporation mechanism of Au in the arsenian pyrite.

Geology of the Shanggong gold deposit

The Shanggong deposit is located in the Xiong'er terrane, southern margin of the North China Craton (Gao and Zhao 2017; Zhao et al. 2018; Fig. 1a). The Xiong'er terrane contains numerous Au deposits hosted in Neoarchean high-grade metamorphic rocks and/or late Paleoproterozoic volcanic rocks (Fig. 1b). Detailed geology and metallogeny of the terrane are available in previous studies (Mao et al. 2002; Chen et al. 2006; Zhao et al. 2018). The Shanggong deposit, the largest Au deposit in the Xiong'er terrane, is located in the northern part of the Kangshan-Qiliping fault (Fig. 1c), and contains more than 30 orebodies that are controlled by the NE-NNE-trending faults (Fig. 1c). The ore-hosting rocks include metamorphic rocks of the Neoarchean-Paleoproterozoic Taihua Complex and the overlying volcanic rocks of the Paleoproterozoic Xiong'er Group. The majority of ore-hosting alteration belts in this

deposit strike northeast and broadly dip 58°-63° NW. Besides, the belts are 700-2200 m long and extend for a few hundred meters down plunge (Chen et al. 2006).

Three stages of mineralization and alteration in this deposit are identified: pre-ore quartz-ankerite alteration (S1), gold-pyritized-phyllite alteration (S2), and late quartz-calcite alteration (S3). The mineral assemblage of the S1 stage comprises quartz, ankerite, and minor epidote and pyrite, and was sheared, mylonitized, and brecciated (Fig. 2a-b), suggesting that the deformation of this assemblage formed under compressional conditions. The S2 stage, the main Au mineralizing stage, is characterized by sericitization, pyritization, and silicification (Fig. 2c-d). Two main types of ores were formed during this stage, including breccia and altered rock-type ores. Pyrite (>5 vol.%, Fig. 2c) is the predominant ore mineral and the most important Au-carrier mineral. Apart from pyrite, the ore minerals also include minor galena and sphalerite (0.1-5 vol.%) and trace chalcopyrite, magnetite, hematite, chalcocite, tetrahedrite, argentite, bornite, pyrrhotite, siderite, electrum, tellurides, and native elements (Au, Ag) (<0.1 vol. %). Commonly, pyrite is crosscut or enclosed by later sphalerite, galena, and trace hessite and electrum (Fig. 2e-h). Gangue minerals are mainly quartz, sericite, and chlorite (Fig. 2c-d), with minor epidote and ankerite. The S3 stage is dominated by quartz-carbonate veinlets, locally containing chlorite, sericite, fluorite, and barite. These veinlets crosscut both mineralized fracture zones and country rocks.

Sampling and analytical methods

The arsenian pyrite grains used for analyses are those closely associated with

stage 2 sericite, quartz, galena, sphalerite, chalcopyrite, chlorite, and ankerite (Fig. 2c-h). In this study, samples were collected in the Exploration Tunnels, and thus are representative ores forming in the main mineralization stage (stage 2). The sampling locations are shown in Electronic Appendix Table A1.

Petrological features and major element compositions of sulfides were determined by scanning electron microscopes (SEM) and EPMA, respectively. Trace element analysis of arsenian pyrite was performed using LA-ICP-MS and Nano secondary ion mass spectroscopy (NanoSIMS). Atomic-scale structural data of arsenian pyrite were obtained by ACSTEM. Furthermore, μ-XANES was utilized to determine the chemical speciation of Au and As in the arsenian pyrite. Detailed descriptions of all the analytical methods are provided in Electronic Appendix.

Results

Textures and compositions of pyrite

According to backscattered electron (BSE) images and EPMA results, three different growth zones of pyrite (Py1, Py2, and Py3) in the S2 stage were identified (Fig. 2e-h). Py1 generally occurs in the core of pyrite grains and rimmed by Py2 (Fig. 2e-f). Py2 is further rimmed by Py3. Py1 contains abundant mineral inclusions and pores (Fig. 2e-f). In some cases, Py2 also contains pores and inclusions of rutile, sphalerite, sericite, quartz, galena, and clay minerals, but in many cases, the mineral inclusions or pores are absent (Fig. 2g-h). Generally, Py3 is almost homogenous and free of any mineral inclusions or pores (Fig. 2e-h). Notably, the zoning of Py2 is parallel to the growing boundary of pyrite (Figs. 2e-h and 4f-g). The contacts between

Py2 and Py3 are sharp and the reaction front is planar and/or curvilinear, which suggests that Py2 was replaced by the ore-forming fluids from which Py3 was deposited.

Py1, Py2, and Py3 formed in stage 2 have different compositions (Figs. 2e-h and 3a). Py2 is richer in Au and As than Py1 and Py3 and has the highest concentrations of Au (up to 0.78 wt%) and As (up to 4.60 wt%) (Table 1). The Au-rich (verified with EPMA) Py2 was selected for LA-ICP-MS analyses and the results confirm that Py2 is rich in As (10291 - 34679 ppm) and Au (1390 - 4823 ppm) (Table 2). Generally, concentrations of other trace metals in Py2 are evidently lower than that of Au and As, such as Zn (<2.71- 57 ppm), Mo (0.28 - 0.51 ppm), Ag (67 - 320 ppm), Cd (0 - 1.40 ppm), Tl (1.12 - 7.75 ppm), Sb (7.58 - 88 ppm), and Pb (28 -210 ppm) (Table 2). Furthermore, concentrations of Se, Sn, Hg, and Bi in Py2 are close to or below the detection limit of LA-ICP-MS.

Based on EMPA BSE and X-ray elemental images (Figs. 2e-f and 4a-c), the Py2 zones are generally 1 to 20 μm in width, As- and Au-rich, and occur as an overgrowth on Py1. Notably, some Py1 domains are also rich in As and Au (Fig. 4b-c), which might be due to overprints of the ore-forming fluids from which have precipitated Py2 (Figs. 2f and 4a-c). The elemental mapping shows that Au concentrations vary inversely with Fe and S and increase with As in Py2 (Fig. 4b-e). Additionally, EMPA results of Py2 show apparent negative correlations of As with S (R^2=0.93) (Fig. 3b) and Au with Fe (R^2=0.82) (Fig. 3c), whereas a positive correlation between As and Au in Py2 (R^2=0.81) is evident (Fig. 3d).

EMPA results show that Py1 has limited variations in Au (bdl-0.03 wt%) and As (bdl-0.94 wt%) contents (Table1). Py3 has similar contents of Au (bdl-0.02 wt%) and As (bdl-0.38 wt%) with Py1. The concentrations of other trace elements in both Py1 and Py3 almost overlap and are broadly similar to those of Py2.

As and Au distribution in arsenian pyrite (Py2)

EPMA mapping with a beam diameter of 1μm shows that the pyrite bears a systematic zoning pattern for As and Au (Fig. 4b-c). To confirm the occurrence of Au and As in arsenian pyrite, high-resolution NanoSIMS mapping with a beam diameter of 250 nm was carried out at the location outlined by the red rectangle in Fig. 4a. The NanoSIMS images reveal that the distributions of Au and As are approximately uniform in Py2 (Fig. 4f-g), suggesting the absence of nanoparticles of Au and/or As-bearing phases in Py2. Furthermore, the LA-ICP-MS time-resolved spectra of Au and As are smooth with only minor and weak spikes (Fig. 5), also indicating that these elements preferably occur as structurally bound phases rather than nanoparticles in Py2 (Large et al. 2007; Cabri and Jackson, 2011).

TEM data of arsenian pyrite (Py2)

The Z-contrast HAADF-STEM images of Au-rich arsenian pyrite show that higher contrasts were detected at the Fe sites as indexed by red arrows (Fig. 6a-b), which is further confirmed by the line profile analysis with evident peaks (Fig. 6d-6e). Its corresponding fast Fourier transformation (FFT) pattern shows a higher degree of crystallinity (Fig. 6c). Besides Fe and S, the TEM energy dispersive X-ray spectrometry (EDS) analyses show that As and Au are the only detected elements in

198 Py2 (Fig. 6f).

199 **As K-edge and Au LIII-edge micro-XANES spectra of arsenian pyrite (Py2)**

200 As K-edge XANES spectra of arsenian pyrite and As-bearing reference materials
201 are shown in Fig. 7. The spectra for different arsenian pyrite grains have analogous
202 characteristics (Fig. 7a), suggesting that the local structure around As is almost the
203 same. A sharp white line peak at 11868 eV is found in the curve of 44J-P5, which is a
204 typical XANES curve of As in arsenian pyrite (Simon et al., 1999a; Cabri et al., 2000).
205 Its energy position is very close to that of FeAsS as As^{-} reference material (Fig. 7b),
206 but far from those of As_2O_3 as As^{3+} reference material and $Na_2HAsO_4 \cdot 7H_2O$ as As^{5+}
207 reference material, which are at 11870 eV and 11874 eV, respectively. This indicates
208 that As in arsenian pyrite bonds as As^{-} instead of As^{3+} or As^{5+}.

209 Au LIII-edge XANES spectra of arsenian pyrite and Au-bearing reference
210 materials, and their first derivative curves are shown in Fig. 8. The XANES spectra
211 analyses on different grains of arsenian pyrite all have analogous characteristics (Fig.
212 8a), suggesting that the local structure around Au is almost the same. The XANES
213 curve of 44J-P3 (Fig. 8b), which is Au in electrum (Fig. 2h), is similar to that of Au
214 foil, indicating Au in electrum occurs as Au^0. However, for all XANES spectra of
215 arsenian pyrite, the two broad peaks observed at 11946 eV and 11969 eV in the
216 XANES curves of Au foil and electrum (Fig. 8b), are not found. The energy positions
217 of the absorption edge of Au foil, representative arsenian pyrite (44J-P5), Au_2S, AuCl,
218 and $AuCl_3$, usually defined as the maximum of the first derivative curve are observed
219 at 11919.0 eV, 11919.5 eV, 11919.4 eV, 11919.6 eV, and 11918.7eV, respectively (Fig.

220 8c).

221 ## Discussion

222 ### Incorporation mechanism of As in arsenian pyrite

223 Although As was traditionally considered to be present as As^- in arsenian pyrite
224 (Simon et al. 1999a; Deditius et al. 2014), cationic As^{3+} (Deditius et al. 2008) and
225 As^{2+} (Qian et al. 2013) also have been documented. Our μ-XANES results suggest
226 that the chemical speciation of As is predominantly present as As^- in the crystal
227 structure of arsenian pyrite (Py2) from the Shanggong deposit. In addition, μ-XANES
228 spectra of different grains of arsenian pyrite are very consistent with each other (Fig.
229 7a), implying the chemical state of As in all arsenian pyrite crystals is univalent anion.
230 The EPMA results have shown a distinct negative correlation between As and S
231 (Fig. 3b), and fairly constant (S + As = 1.9997 (apfu)) content approaching
232 stoichiometry with a variance of σ=0.0004 in Py2 (Electronic Appendix Table A4).
233 These features indicate a substitution of S by As in the arsenian pyrite structure.
234 Similarly, a strong negative correlation between S and As has been reported in pyrite
235 from Carlin Au, porphyry Cu–Au, and epithermal Au, orogenic Au, volcanogenic
236 massive sulfide (VHMS), iron-oxide Cu–Au (IOCG) and Witwatersrand modified
237 paleoplacer Au deposits (Deditius et al. 2014; Pokrovski et al. 2014 and references
238 therein). Moreover, the ratios of the decrease of S atoms to the increase of As atoms
239 per formula unit (N_{2-S}/N_{As}) range from 1.00 to 1.03 with an average value of 1.01 and
240 variance of σ=0.01 (Electronic Appendix Table A4), which further indicates that one
241 As substituted one S in the pyrite lattice. It is also well shown in the μ-XANES

242 spectra that the chemical speciation of As in arsenian pyrite is dominant As^{-}. We thus
243 conclude that As was incorporated into Py2 structure through a substitution of S by
244 As^{-} in the S_{2-2} unit to form $(S_{2-x}, As_x)_{2-2}$, this mechanism is commonly documented in
245 previous studies (Cook and Chryssoulis 1990; Simon et al. 1999a, 1999b; Savage et al.
246 2000; Pals et al. 2003; Liang et al. 2013).

247 **Occurrence of Au in arsenian pyrite**

248 Elemental mapping by EPMA and NanoSIMS and LA-ICP-MS time-resolved
249 spectra discussed above show that both Au and As are broadly homogenously
250 distributed in Au-rich arsenian pyrite (Fig. 4b-c), suggesting that the two elements are
251 mainly bonded in the structure of arsenian pyrite from the Shanggong deposit.

252 The Z-contrast HAADF-STEM image is a powerful method to identify not only
253 the atomic arrangement but also trace elemental substitution within crystal lattice in
254 sub-angstrom resolution with an ACSTEM (Lee et al. 2016; Liao et al. 2019), thus
255 useful for exploring the Au occurrence in arsenian pyrite at the atomic-scale.
256 ACSTEM observations show higher contrasts at the Fe sites of the arsenian pyrite
257 (Fig. 6a-b), which is further confirmed by the line profile analysis with evident peaks
258 (Fig. 6d-e). In theory, the intensity of HAADF-STEM images is roughly proportional
259 to the square of the atomic number and number of atoms along the beam direction in
260 Z-contrast images (Liao et al. 2019). This means that the brighter spots in Fig. 6a-b
261 indicate substitution of Fe by some heavy elements in the pyrite lattice. Indeed, the
262 TEM-EDS spectrum suggests the existence of Au and As in the arsenian pyrite crystal
263 (Fig. 6f), and the EPMA and LA-ICP-MS results confirm that the arsenian pyrite

grains are relatively rich in Au but depleted in other metals (e.g. Zn, Ni, Co, Ag, Te, Cu, Sb, and Pb; Tables 1 and 2). This allows us to propose that the heavy elements preferably are Au, as the atomic number of Au (Z=79) is much larger than those of Fe (Z=26), As (Z=33), and S (Z=16).

Chemical state of Au in arsenian pyrite

XANES spectrum is very sensitive to the state of elements (Simon et al. 1999a; Filimonova et al., 2020, and references therein). However, the low concentration and the heterogeneity of Au in arsenian pyrite make it very difficult to obtain high-quality Au L_{III}-edge XANES spectra (Merkulova et al. 2019; Pokrovski et al. 2019; Filimonova et al. 2020). Such a situation is further enlarged by the presence of As because the As Kα line is seriously overlapped with the Au Lα line. Given these facts, we carried out μ-XANES analyses on the arsenian pyrite that is relatively rich in Au. Moreover, these studied arsenian pyrites are depleted in other elements (e.g. Zn, Ni, Co, Ag, Cu, and Pb, Tables 1 and 2), in particular, Sb, Te, and Bi are possible coordinated with Au. The XANES spectra for Au in arsenian pyrite show a white line peak at ~11922 eV and the absence of the two broad peaks at 11946 eV and 11969 eV (Fig. 8a), implying that the Au speciation is not metal state but chemically bound Au. Besides, the XANES spectra for Au in arsenian pyrite are consistent with each other and the absorption edge of the representative μ-XANES spectrum is very close to that of Au_2S and AuCl but relatively far from that of $AuCl_3$ (44J-P5, Fig. 8c), suggesting that Au in arsenian pyrite probably mainly occurs as Au^+. Our work is consistent with recent studies of high-quality XANES using the HERFD-XAS technique (Merkulova

et al. 2019; Pokrovski et al. 2019; Filimonova et al. 2020).

Incorporation mechanism of Au in arsenian pyrite

On the basis of elemental correlations, available chemical state, and nanoscale structure of Au, several incorporation mechanisms of structurally bound Au in pyrite have been proposed. Some studies suggested that Au is adsorbed on the As-rich, Fe-deficient surface of arsenian pyrite, and such a process is able to be enhanced by As incorporation (Sha 1993; Fleet and Mumin 1997; Simon et al. 1999b; Pals et al. 2003). In contrast, most studies argued that the structurally bound Au should be incorporated into arsenian pyrite by coupled substitution of cationic Fe in distorted arsenian pyrite due to the substitution of S by anionic As in the mineral (Arehart et al. 1993; Chouinard et al. 2005; Deditius et al. 2008). Arehart et al. (1993) suggested that Au was probably incorporated into arsenian pyrite as Au^{3+} at the Fe site through coupled substitution with As^{-} at the S site by the model of $(Au_x^{3+}, Fe_{1-x}^{2+}), ([AsS^{3-}]_x, [S_2^{2-}]_{1-x})$. Other possible substitution models for Au and As in pyrite were also proposed, including $Au^{3+} + Cu^{+} \leftrightarrow 2Fe^{2+}$ (Chouinard et al. 2005), $As^{3+} + yAu^{+} + (1-y)\square \leftrightarrow 2Fe^{2+}$ and $As^{3+} + Au^{3+} + \square \leftrightarrow 3Fe^{2+}$ (Deditius et al. 2008).

In this study, our new results of EPMA and NanoSIMS mapping (Fig. 4b-g) and LA-ICP-MS time-resolved spectrum (Fig. 4h) indicate that Py2 is relatively rich in Au and As (Table 1) but depleted in other elements (Tables 1 and 2), and that Au and As occur as chemically bound phases in their carrier. As discussed in the previous section, Au occurs overwhelmingly as chemically bound Au^{+} in arsenian pyrite (Py2).

Considering the large ionic size of Au^{+} (0.137 nm), earlier studies proposed that Au is incorporated into the arsenian pyrite structure in vacancy or defect positions rather than directly substituting for Fe^{2+} (0.061 nm) (Cook and Chryssoulis 1990; Fleet and Mumin 1997). Moreover, Pokrovski et al. (2019) proposed that chemically bound Au^{+} mainly occurs in sulfide clusters composed of Au_2S linear units rather than Fe or S atom sites in the structure of As-free pyrite. In contrast, recent spectroscopy studies of Au in pyrite using HERFD-XAS suggest that chemically bound Au^{+} occupies the Fe site (Trigub et al. 2017; Merkulova et al. 2019; Filimonova et al. 2020). Moreover, our new results of the [100] zone axis Z-contrast images of Au-rich arsenian pyrite suggest that Au atoms probably occupy the Fe atom sites (Fig. 6a-b), further confirming that Au atoms might directly substitute Fe atoms in the studied arsenian pyrite.

The local atomic environment of Au is the key factor to investigate Au incorporation in pyrite. Generally, the formal oxidation states of Fe and S in pyrite are traditionally regarded as +2 and -1, respectively. Considering the conservation law of charge, the amount of Au^{+} in arsenian pyrite of the Shanggong deposit is not high enough to balance the deficit of positive charge connected with a substitution of Au^{+} for Fe^{2+}. As such, the charge imbalance may be compensated by anionic vacancies with a coupled substitution:

$$Au^{+} + \square \leftrightarrow Fe^{2+} + S^{-}/[As^{-}] \quad (1)$$

where $[As^{-}]$ and ($\square$) represent an As atom occupying at the S atom site and an anionic vacancy, respectively. However, recent spectroscopic results indicate that

structurally bound Au is covalently bonded with 6 S (Merkulova et al. 2019; Filimonova et al. 2020), suggesting that anionic vacancies are less likely to be formed in the nearest shell around Au atoms in pyrite structure. Moreover, the Fe-S bonds in pyrite structure possess both ionic and covalent character and the S-S bonds show strong covalent peculiarity (Schmøkel et al. 2014). In other words, pyrite is a mineral with highly covalent chemical bonds. This suggests that the above deficit of positive charge may be compensated by the partial electron transfers of atoms, rather than the formation of anionic vacancies on the S atom sites in pyrite structure (Schmøkel et al. 2014; Trigub et al. 2017). In summary, chemically bound Au^{+} was incorporated into arsenian pyrite via a substitution of Au for Fe in the structure of the mineral. Nevertheless, the accurate coordination of Au in arsenian pyrite of this study needs to be further studied using HERFD-XAS and crystal structure determinations.

The role of As on the enrichment of Au in arsenian pyrite remains unclear. The positive correlation between the structurally bound Au and As in pyrite from different types of ore deposits has been widely reported (Pals et al. 2003; McClenaghan and Lentz 2004; Reich et al. 2005; Deditius et al. 2008; Muntean et al. 2011; Agangi et al. 2013; Deditius et al. 2014 and this study (Fig. 3d)), implying that the distribution and incorporation of Au in arsenian pyrite are closely related to As. Recent experimental studies demonstrated that Au incorporation in pyrite is largely dependent on As enrichment and a prolonged fluid-rock interaction rather than an anomalously Au-rich ore-forming fluid (Kusebauch et al. 2019; Xing et al. 2019). As a result, we propose that the pyrite with higher As tends to have higher Au, in other words, the

352 incorporation of As in pyrite could provide a favorable structural environment for the
353 incorporation of Au. However, some other studies found that Au and As do not have a
354 pronounced correlation and thus proposed that incorporation of the structurally bound
355 Au in their studied pyrite is independent of As (Trigub et al. 2017; Merkulova et al.
356 2019; Filimonova et al. 2020 and references therein). Rather, the Au on the Fe site is
357 only coordinated with S atoms (Filimonova et al. 2020). Moreover, these authors
358 proposed that the correlation between Au and As should be related to the occurrence
359 of the Au-bearing arsenopyrite or löllingite-like clusters/inclusions in pyrite, and/or
360 the simultaneously increasing As and Au dissolved in the ore-forming fluids (Trigub
361 et al. 2017; Filimonova et al. 2020). Pokrovski et al. (2019) proposed that Au
362 incorporation is independent of As content in As-poor pyrite but facilitated by
363 increasing As content in As-rich pyrite. These results imply that As might be
364 beneficial rather than necessary for the incorporation of chemically bound Au in
365 pyrite. In view of the diversity of natural samples, more comprehensive studies are
366 necessary to reveal the role of As on the incorporation of Au in arsenian pyrite.

367 **Implication**

368 Arsenian pyrite is one of the most common structurally bound Au-hosting
369 minerals in hydrothermal ore deposits. The incorporation mechanism of structurally
370 bound Au in pyrite has been extensively investigated, but the accurate mechanism
371 remains poorly understood. Combining a comprehensive chemical and atomic-scale
372 structural study on Au-bearing arsenian pyrite, we propose that the chemically bound
373 Au^{+} was incorporated into arsenian pyrite of this study via a substitution of Au^{+} for

374 Fe^{2+} in the lattice of the mineral. Moreover, our study suggests that As could be a
375 favorable rather than necessary condition for the incorporation of structurally bound
376 Au in pyrite. Notably, our findings have important significance for exploring the
377 process by which Au was enriched from ore-forming fluids with low Au and As
378 concentrations into arsenian pyrite of hydrothermal ore deposits such as Carlin,
379 epithermal, and orogenic Au deposits. Additionally, this study can serve as a
380 reference for investigating the occurrence, chemical state, and incorporation
381 mechanism of structurally bound other scatter and noble metals (e.g. PGE, Ag, Co)
382 in their host sulfides.

383 **Acknowledgments**

384 We thank Qiang Wu, Qiang Zhan, Yifan Qiu, Yiping Yang, and Junming Zhou
385 for their assistance with the field and the laboratory work. We are grateful to Meifu
386 Zhou, Jianxi Zhu, and Alexandra Yang Yang for their help with the preparation of this
387 paper. The authors acknowledge Fang-Yue Wang for his help with LA-ICP-MS
388 analyses. Rosa Anna Fregola, Michalis Fitros, Louis J. Cabri and an anonymous
389 reviewer are greatly appreciated for their constructive reviews. Sasa Bajt is gratefully
390 acknowledged for his editorial handling. The authors thank the SSRF for the
391 beamtime allocation under the proposal No. 2018-SSRF-PT-005554. This work was
392 financially supported by the National Key Research and Development Program of
393 China (Grant Nos. 2016YFC0600106 and 2016YFC0600408).

394 **References**

Agangi, A., Hofmann, A., and Wohlgemuth-Ueberwasser, C.C. (2013) Pyrite Zoning as a Record of Mineralization in the Ventersdorp Contact Reef, Witwatersrand Basin, South Africa. Economic Geology, 108, 1243-1272.

Arehart, G.B., Chryssoulis, S.L., and Kesler, S.E. (1993) Gold and Arsenic in Iron Sulfides from Sediment-hosted Disseminated Gold Deposits-Implications for Depositional Processes. Economic Geology, 88, 171-185.

Cabri, L.J. and Jackson, S.E. (2011) New developments in characterization of sulphide refractory gold ores. World Gold 2011, Proceedings 50th Annual Conference of Metallurgists (eds. Deschênes, G., Dimitrakopolous, R., Bouchard, J.), Montreal, 51-62.

Cabri, L.J., Gordon, R.A., Crozier, E.D., Sutton, S.R., Mcmahon, G., and Jiang, D. (2000) Chemical speciation of gold in arsenopyrite. Canadian Mineralogist, 38, 1265-1281.

Chen, Y.J., Pirajno, F., Qi, J.P., Li, J., and Wang, H.H. (2006) Ore geology, Fluid Geochemistry and Genesis of the Shanggong Gold Deposit, Eastern Qinling Orogen, China. Resource Geology, 56, 99-116.

Chouinard, A., Paquette, J., and Williams-Jones, A.E. (2005) Crystallographic controls on trace-element incorporation in auriferous pyrite from the Pascua epithermal high-sulfidation deposit, Chile-Argentina. Canadian Mineralogist, 43, 951-963.

Cline, J.S. (2001) Timing of Gold and Arsenic Sulfide Mineral Deposition at the Getchell Carlin-Type Gold Deposit, North-Central Nevada. Economic Geology,

96, 75-89.

Cook, N.J. and Chryssoulis S.L. (1990) Concentrations of "invisible gold" in the common sulfides. Canadian Mineralogist, 28, 1-16.

Deditius, A.P., Reich, M., Kesler, S.E., Utsunomiya, S., Chryssoulis, S.L., Walshe, J. and Ewing, R.C. (2014) The coupled geochemistry of Au and As in pyrite from hydrothermal ore deposits. Geochimica et Cosmochimica Acta, 140, 644-670.

Deditius, A.P., Utsunomiya, S., Renock, D., Ewing, R.C., Ramana, C.V., Becker, U. and Kesler, S.E. (2008) A proposed new type of arsenian pyrite: Composition, nanostructure and geological significance. Geochimica et Cosmochimica Acta, 72, 2919-2933.

Filimonova, O.N., Tagirov B.R., Trigub, A.L., Nickolsky, M.S., Rovezzi, M.R., Belogub, E.V., Reukov, V.L., and Vikentyev, I.V. (2020) The state of Au and As in pyrite studied by X-ray absorption spectroscopy of natural minerals and synthetic phases. Ore Geology Reviews, 121. DOI:10.1016/j.oregeorev. 2020.103475.

Fleet, M.E. and Mumin, A.H. (1997) Gold-bearing arsenian pyrite and marcasite and arsenopyrite from Carlin Trend gold deposits and laboratory synthesis. American Mineralogist, 82, 182-193.

Gao, X.Y. and Zhao, T.P. (2017) Late Mesozoic magmatism and tectonic evolution in the Southern margin of the North China Craton. Science China Earth Sciences, 60, 1959-1975.

Huergo, M.A., Giovanetti, L.J., Rubert, A.A., Grillo, C.A., Moreno, M.S., Requejo,

F.G., Salvarezza, R.C. and Vericat, C. (2019) The surface chemistry of near-infrared resonant gold nanotriangles obtained via thiosulfate synthesis. Applied Surface Science, 464, 131-139.

Kusebauch, C., Gleeson, S.A. and Oelze, M. (2019) Coupled partitioning of Au and As into pyrite controls formation of giant Au deposits. Science Advances, 5, 1-8.

Large, R.R., Maslennikov, V.V., Robert, F., Danyushevsky, L.V. and Chang, Z. (2007) Multistage Sedimentary and Metamorphic Origin of Pyrite and Gold in the Giant Sukhoi Log Deposit, Lena Gold Province, Russia. Economic Geology, 102, 1233-1267.

Lee, S., Shen, Z.Z. and Xu, H.F. (2016) Study on nanophase iron oxyhydroxides in freshwater ferromanganese nodules from Green Bay, Lake Michigan, with implications for the adsorption of As and heavy metals. American Mineralogist, 101, 1986-1995.

Liang, J.L., Sun, W.D., Li, Y.L., Zhu, S.Y., Li, H., Liu, Y.L. and Zhai, W. (2013) An XPS study on the valence states of arsenic in arsenian pyrite: Implications for Au deposition mechanism of the Yang-shan Carlin-type gold deposit, western Qinling belt. Journal of Asian Earth Sciences, 62, 363-372.

Liao, J.L., Sun, X.M., Li, D.F., Sa, R., Lu, Y., Lin, Z.Y., Xu, L., Zhan, R., Pan, Y.G. and Xu, H.F. (2019) New insights into nanostructure and geochemistry of bioapatite in REE-rich deep-sea sediments: LA-ICP-MS, TEM, and Z-contrast imaging studies. Chemical Geology, 512, 58-68.

Mao, J.W., Goldfarb, R., Zhang, Z.W., Xu, W.Y., Qiu, Y.M. and Deng, J. (2002)

461 Gold deposits in the Xiaoqinling-Xiong'ershan region, Qinling Mountains,
462 central China. Mineralium Deposita, 37, 306-325.
463 McClenaghan, S.H. and Lentz, D.R. (2004) Abundance and speciation of gold in
464 massive sulfides of the Bathurst mining camp, New Brunswick, Canada.
465 Canadian Mineralogist, 42, 851-871.
466 Merkulova, M., Mathon, O., Glatzel, P., Rovezzi, M., Batanova, V., Marion, P.,
467 Boiron, M.C. and Manceau, A. (2019) Revealing the Chemical Form of
468 “Invisible” Gold in Natural Arsenian Pyrite and Arsenopyrite with High
469 Energy-Resolution X‐ray Absorption Spectroscopy. ACS Earth and Space
470 Chemistry, 3, 1905-1914.
471 Momma, K. and Izumi, F. (2008) VESTA: a three-dimensional visualization system
472 for electronic and structural analysis. Journal of Applied Crystallography, 41,
473 653–658.
474 Muntean, J.L., Cline, J.S., Simon, A.C. and Longo, A.A. (2011) Magmatic–
475 hydrothermal origin of Nevada’s Carlin-type gold deposits. Nature Geoscience, 4,
476 122-127.
477 Newville, M. (2001) IFEFFIT: interactive XAFS analysis and FEFF fitting. Journal of
478 Synchrotron Radiation, 8, 322-324.
479 Palenik, C.S., Utsunomiya, S., Reich, M., Kesler, S.E., Wang, L. and Ewing, R.C.
480 (2004) "Invisible" gold revealed: Direct imaging of gold nanoparticles in a
481 Carlin-type deposit. American Mineralogist, 89, 1359-1366.
482 Pals, D.W., Spry, G.G. and Chryssoulis, S. (2003) Invisible Gold and Tellurium in

Arsenic-Rich Pyrite from the Emperor Gold Deposit, Fiji: Implications for Gold Distribution and Deposition. Economic Geology, 98, 479-493.

Pokrovski, G.S., Akinfiev, N.N., Borisova, A.Y., Zotov, A.V. and Kouzmanov, K. (2014) Gold speciation and transport in geological fluids: Insights from experiments and physical-chemical modeling. Geological Society, London, Special Publication, 402, 9-70.

Pokrovski, G.S., Kokh, M.A., Proux, O., Hazemann, J.L., Bazarkina, E.F., Testemale, D., Escoda, C., Boiron, M.C., Blanchard, M., Aigouy, T., Gouy, S., Parseval, P. and Thibaut, M. (2019) The nature and partitioning of invisible gold in the pyrite-fluid system. Ore Geology Reviews, 109, 545-563.

Qian, G., Brugger, J., Testemale, D., Skinner, W. and Pring, A. (2013) Formation of As(II)-pyrite during experimental replacement of magnetite under hydrothermal conditions. Geochimica et Cosmochimica Acta, 100, 1-10.

Reich, M., Kesler, S.E., Utsunomiya, S., Palenik, C.S., Chryssoulis, S.L. and Ewing, R.C. (2005) Solubility of gold in arsenian pyrite. Geochimica et Cosmochimica Acta, 69, 2781-2796.

Savage, K.S., Tingle, T.N., O'Day, P.A., Waychunas, G.A. and Bird, D.K. (2000) Arsenic speciation in pyrite and secondary weathering phases, Mother Lode Gold District, Tuolumne County, California. Applied Geochemistry, 15, 1219-1244.

Schmøkel, M.S., Bjerg, L., Cenedese, S., Jørgensen, M.R.V., Chen, Y.S., Overgaard, J., and Iversen, B.B. (2014) Atomic properties and chemical bonding in the

pyrite and marcasite polymorphs of FeS_2: A combined experimental and theoretical electron density study. Chemical Science, 5, 1408-1421.

Sha, P. (1993) Geochemistry and genesis of sediment-hosted disseminated gold mineralization at the Gold Quarry mine, Nevada. Ph. D. thesis, University. Alabama, Tuscaloosa, p. 228.

Simon, G., Huang, H., Penner-Hahn, J.E., Kesler, S.E. and Kao, L.S. (1999a) Oxidation state of gold and arsenic in gold-bearing arsenian pyrite. American Mineralogist, 84, 1071-1079.

Simon, G., Kesler, S.E. and Chryssoulis, S. (1999b) Geochemistry and Textures of Gold-Bearing Arsenian Pyrite, Twin Creeks, Nevada: Implications for Deposition of Gold in Carlin-type Deposit. Economic Geology, 94, 405-422.

Sung, Y.H., Brugger, J., Ciobanu, C.L., Pring, A., Skinner, W. and Nugus, M. (2009) Invisible gold in arsenian pyrite and arsenopyrite from a multistage Archaean gold deposit: Sunrise Dam, Eastern Goldfields Province, Western Australia. Mineralium Deposita 44, 765-791.

Trigub, A.L., Tagirov, B.R., Kvashnina, K.O., Chareev, D.A., Nickckolsky, M.S., Shiryaev, A.A., Baranova, N.N., Kovalchuk, E.V., and Mokhov, A.V. (2017) X-ray spectroscopy study of the chemical state of “invisible” Au in synthetic minerals in the Fe-As-S system. American Mineralogist, 102, 1057-1065.

Xing, Y.L., Brugger, J., Tomkins, A. and Shvarov, Y.R. (2019) Arsenic evolution as a tool for understanding formation of pyritic gold ores. Geology, 47, 335-338.

Zhao, T.P., Meng, L., Gao, X.Y., Jin, C., Wu, Q. and Bao, Z.W. (2018) Late

Mesozoic felsic magmatism and Mo-Au-Pb-Zn mineralization in the southern margin of the North China Craton: A review. Journal of Asian Earth Sciences, 161, 103-121.

Figure captions

Fig. 1 (a) Major Tectonic outlines of China and (b) Geological map showing major deposits in the Xiong'er terrane, the southern margin of the North China Craton (modified after Zhao et al. 2018); (c) Geological map of the Shanggong deposit (modified from a 1:10,000-scale geologic map).

Fig. 2 (a) Typical orebody. Quartz (ankerite) vein was cross-cut by quartz-sericite-pyrite vein. (b) Representative brecciated ore, in which the quartz (ankerite) breccias are surrounded by quartz-sericite-pyrite vein. (c-d) Alteration of quartz-sericite-pyrite. (e-h) BSE images show the paragenesis of pyrite. Py1 generally occurs as core overgrown by Py2. The Py2 is further overgrown by Py3. The Py1 contains abundant mineral inclusions and pores and was locally corroded or replaced Py2. In some cases, the Py2 zones also contain pores and inclusions of rutile, sericite, quartz, galena, and others, but in many cases, they are absent of the mineral inclusions or pores. Generally, Py3 is homogenous and free of any pores or mineral inclusions. (f) An altered Py1 shown by a white arrow might be replaced by a later ore-fluid forming Py2 (Fig. 2e). (g-h) Fractures in Py1-3 are filled by sphalerite (Sph), galena (Gn), and trace hessite (Hes) and electrum (Elc). The area marked by the red rectangle in Fig. 2g

549 is the sampling location (T5) for TEM analyses. Abbreviations: Q-quartz,
550 Ank-ankerite, Ser-sericite, Py-pyrite, Py1-euhedral Au, As-poor pyrite, Py2- Au-rich
551 arsenian pyrite, Py3-Au, As-poor pyrite.
552
553 Fig. 3 EPMA analyses of Py1-3 (in at.%) from the Shanggong deposit (Electronic
554 Appendix Table A3). (a) Ternary Fe-S-As diagram for Py1-3 (b). S vs. As diagram for
555 Py2. (c) Fe vs. Au diagram for Py2; (d) As vs. Au diagram for Py2.
556
557 Fig. 4 (a-e) Back-scattered electron image associated with X-ray element mappings of
558 $As_{L\alpha}$, $Au_{M\alpha}$, $Fe_{K\alpha}$ and $S_{K\alpha}$ obtained by EPMA. (f-g) NanoSIMS mapping images of
559 $^{75}As^{32}S$ and ^{197}Au for the area labeled with the red rectangle shown in Fig. 4a. The
560 intensity of color was enhanced to show the inverse relationship between As and S
561 and Au and Fe and does not represent actual concentrations of the analyzed elements.
562
563 Fig. 5 LA-ICP-MS time-resolved spectra of spot analyses for the Au-rich arsenian
564 pyrite (Py2). Note: The stable Fe time-resolved spectrum becomes sharp outside the
565 red dashed rectangular box (Figs. 5a, 5e, and 5f), which might be caused by
566 micro-inclusions in the Py2 or its fractures. Additionally, the Fe signal intensity starts
567 to drop rapidly outside the box (Fig. 5b-d), suggesting that the Py2 was punctured.
568 Thus, we chose the spectra marked by the box as the research object to explore the
569 occurrence of Au and As in Py2.
570

571 Fig. 6 TEM analyses. (a) A large area [100] zone axis Z-contrast micrograph of Py2,
572 its location (T5) is shown in Fig. 2g. (b) A Z-contrast image with the pyrite atomic
573 model in the upper left. The red and yellow balls represent Fe and S atom,
574 respectively. The Z-contrast image demonstrates an Au substitution at the Fe atom site
575 with atomic resolution as significant from a brighter contrast. (c) The associated FFT
576 pattern image. (d-e) The intensity profiles of the marked lines in Fig. 6a. The labeled
577 stronger peaks are associated with Fe columns with substituted heavy atoms of Au. (f)
578 The corresponded EDS spectrum for the arsenian pyrite of Fig. 6a.
579
580 Fig. 7 XANES spectrum for As in arsenian pyrite, and standard compounds of FeAsS
581 (As^{-}), As_2O_3 (As^{3+}), and $Na_2HAsO_4 \cdot 7H_2O$ (As^{5+}).
582
583 Fig. 8 (a-b) XANES spectrum for Au in arsenian pyrite (Py2), electrum (44J-P3), and
584 standard compounds of Au foil (Au^0, this study), Au_2S (Au^+, Pokrovski et al. 2019),
585 AuCl (Au^+, Huergo et al. 2019) and $AuCl_3$ (Au^{3+}, Huergo et al. 2019). (c) The first
586 derivative of Au L_{III}-edge XANES for Au foil, 44J-P5, AuCl, Au_2S and $AuCl_3$.

Table 1 EPMA data for Py1, Py2 and Py3 (in wt%)

Sample	Au	As	S	Fe	Zn	Ni	Co	Ag	Te	Cu	Sb
Py2(n=47)											
Average	0.30	2.64	51.36	45.45	0.01	bdl	0.07	0.01	0.02	0.07	bdl
Maximum	0.78	4.60	53.08	46.45	0.05	0.01	0.09	0.13	0.13	0.27	0.02
Minimum	0.05	0.39	50.02	44.37	bdl	bdl	0.03	bdl	bdl	bdl	bdl
Py1(n=11)											
Average	bdl	0.28	53.51	46.40	bdl	0.02	0.05	bdl	0.02	bdl	bdl
Maximum	0.03	0.94	54.24	46.81	0.02	0.03	0.06	0.01	0.07	0.01	0.02
Minimum	bdl	bdl	52.50	45.82	bdl	bdl	0.03	bdl	bdl	bdl	bdl
Py3(n=14)											
Average	bdl	bdl	53.93	46.36	bdl	0.03	0.05	bdl	0.02	0.03	bdl
Maximum	0.02	0.38	54.69	46.68	0.02	0.07	0.07	bdl	0.08	0.29	0.03
Minimum	bdl	bdl	52.90	45.54	bdl	bdl	0.03	bdl	bdl	bdl	bdl

Note: (1) bdl denotes below detection limit; (2) Hg, Pb, Bi, Se, close to or below detection limit; (3) The whole dataset is listed in Electronic Appendix Table A2. (4) The reported mean concentrations for elements were calculated as half of the detection limit.

Table 2 LA-ICP-MS data for Py2 (in ppm)

Sample No.	Analysis No.	As	Au	Ag	Co	Ni	Cu	Zn	Se	Mo	Cd	Sn	Sb	Hg	Tl	Pb	Bi
SG44J-T1-rg1	Spot-21	10291	1390	67	77	125	759	<5.98	<51	0.28	0.39	<0.36	23	0.91	3.97	94	0.0012
SG44J-T1-rg2	Spot-25	34679	3113	320	802	313	1417	46	<53	0.43	0.00	<0.36	88	0.57	7.75	37	0.0066
SG44J-T1-rg3	Spot-34	26447	3164	139	201	162	1884	57	<30	0.51	0.85	<0.25	30	0.55	2.87	210	<0.0022
SG44J-T1-g1	Spot-41	21274	2735	87	450	262	592	2.60	<29	0.31	0.00	<0.34	25	0.56	4.52	136	<0.0019
SG44J-T1-g2	Spot-44	17110	2609	170	496	489	789	<2.71	<33	0.49	<1.20	<0.34	7.58	<0.51	1.12	28	<0.0029
SG44J-T1-g5	Spot-48	31032	4823	130	26	32	1139	<4.55	<33	0.35	<1.40	<0.27	19	<0.51	2.56	68	<0.0049

Fig. 1

a

Central Asian Orogen

Central Asian Orogen

Tarim Craton

Kunlun-Qinling-Dabie orogen

North China Craton

Fig. b

Qinghai-Tibet plateau

Yangtze Craton

Cathaysia block

800 km

b

N

0 5 10km

Luoning fault

Huashan

N34°20'

Fig. 1c

Luoning fault

Haopinggou

Shagou

Tieluping

Shanggong

Wuzhangshan

Leimengou

Qiyugou

Huanxiangwa

Jiaoyuan fault

Taocun-Mayuan fault

N34°10'

Kangshan-Qiliping fault

Kangshan

Beiling

Huaishuping

Machaoying fault

Tantou basin

Miaoling

Qianhe

Machaoying fault

Yuchiling

E111°15'

E111°30'

E111°45'

Heyu

c

N

0 0.5 1km

Hugou mining district

M22

M19

M12

M16

A

B

F5

F1

M35

F1

Old Shanggong mining district

Ganshu mining district

Late Archean Taihua Complex

Paleoproterozoic volcanic rocks of Xiong'er Group

Xushan Formation andesite

Jidanping Formation dacite

Mesoproterozoic Guandaokou Group clastic and carbonate rocks

Mesoproterozoic Luanchuan Group clastic and carbonate rocks

Cretaceous to Cenozoic sediments

Mesozoic granitoid intrusion

Unconformity surface

Faults

Sampling location

Au-bearing Faults

Molybenum deposits

Gold deposits

Ag-Pb-Zn deposits

Fig. 2

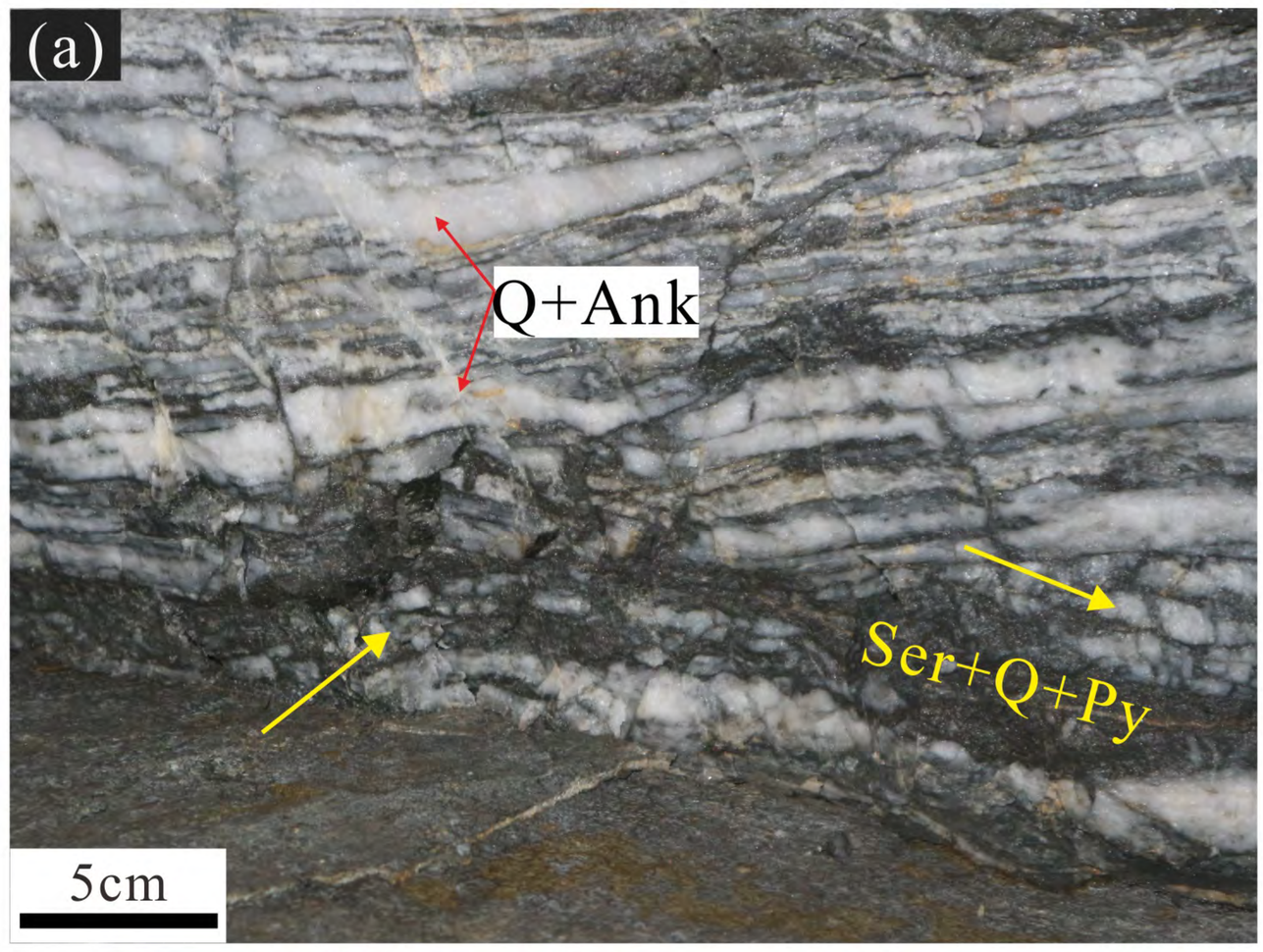
(a)
Q+Ank
Ser+Q+Py
5cm


(b)
Ser+Q+Py
Q
Ser+Q+Py
2cm

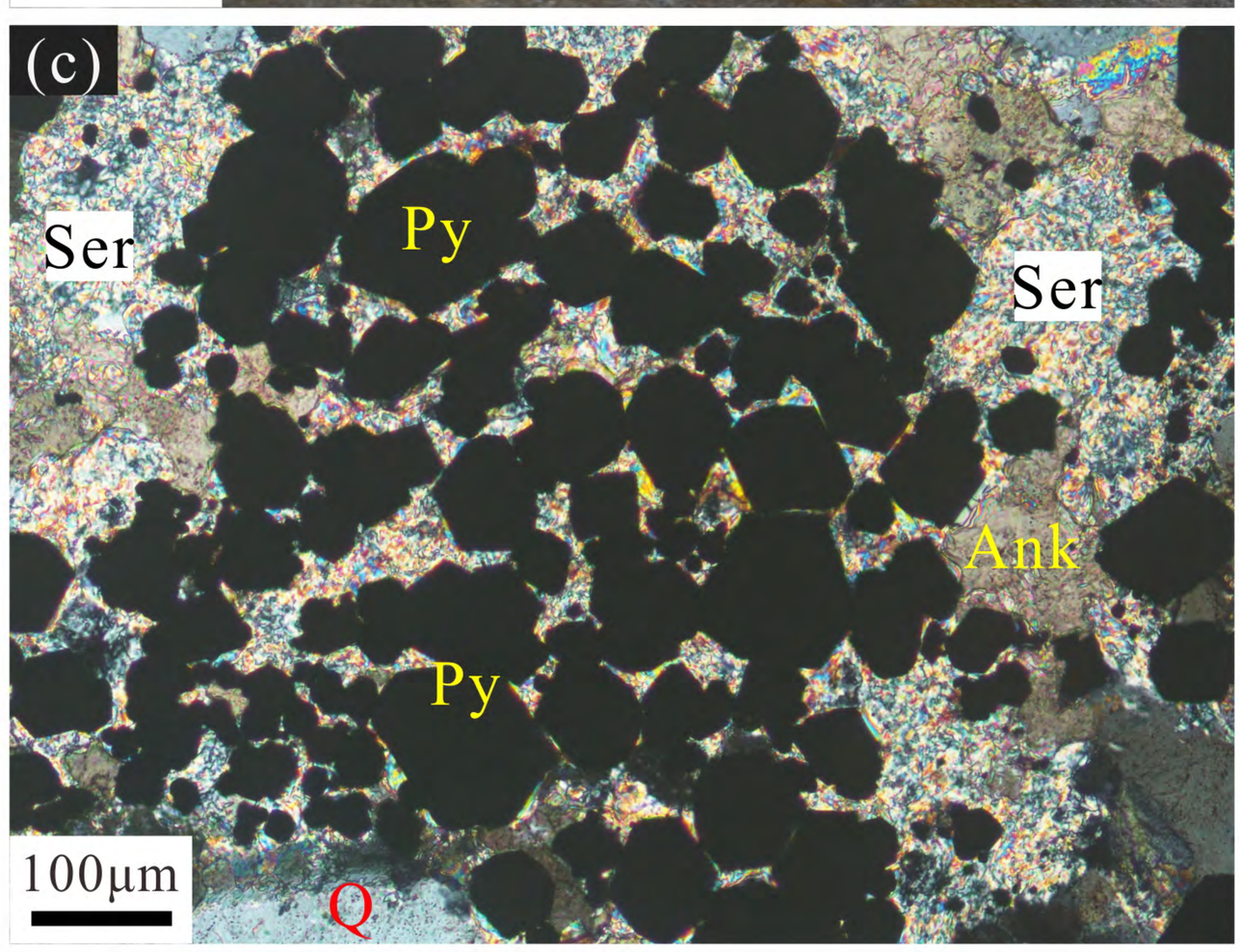
(c)
Ser
Py
Ser
Ank
Py
Q
100μm

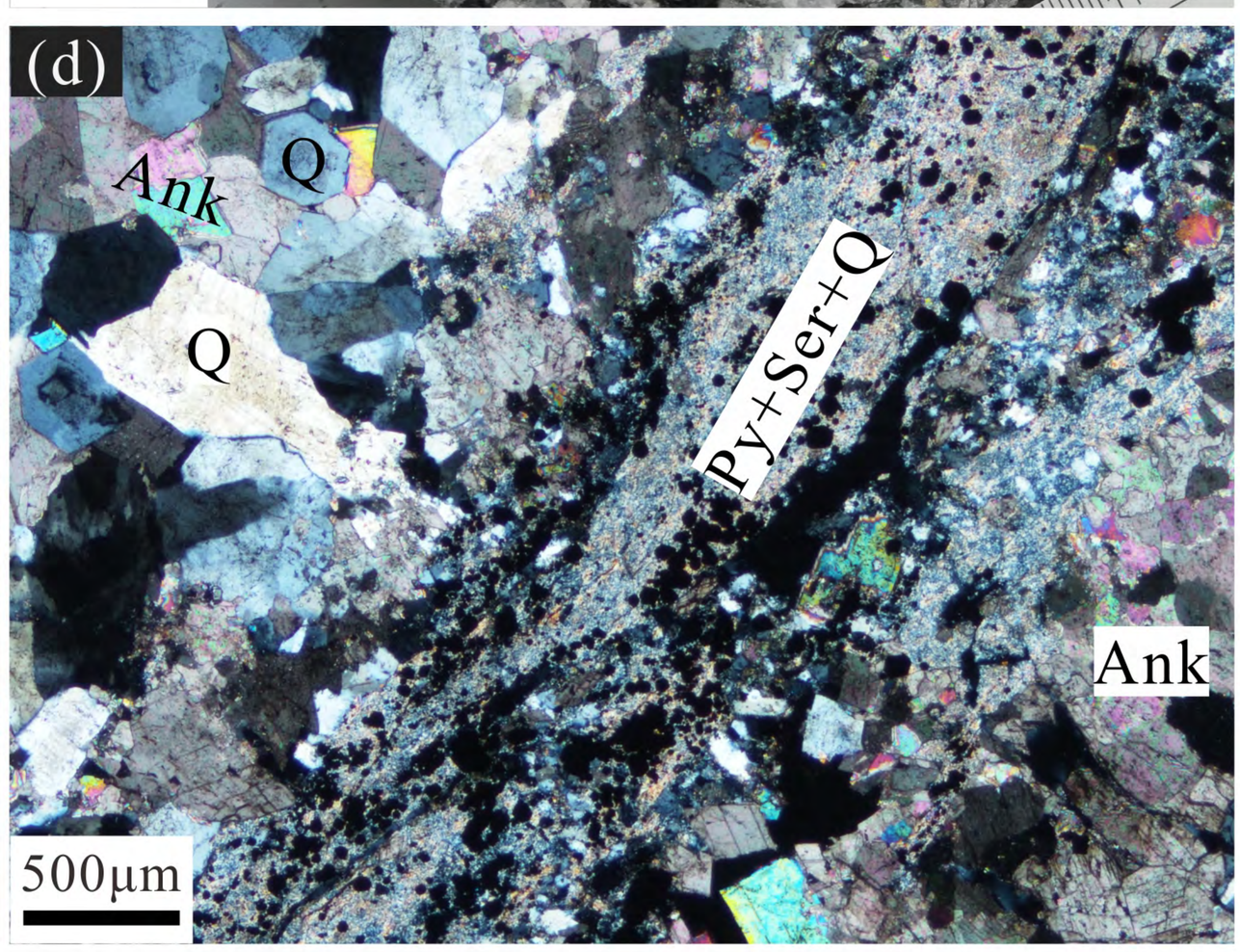
(d)
Ank
Q
Q
Py+Ser+Q
Ank
500μm

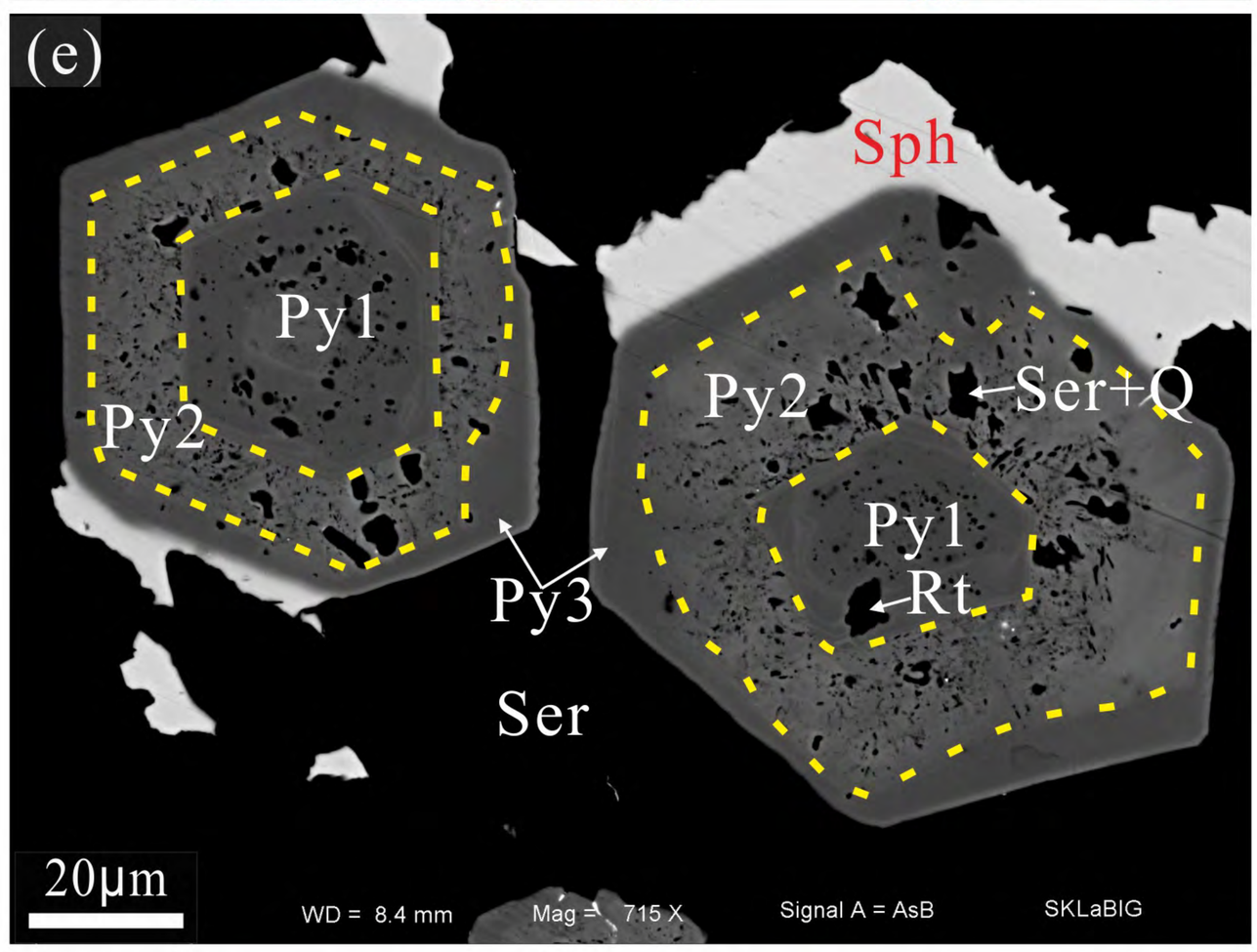
(e)
Sph
Py1
Py2
Py2
←Ser+Q
Py1
←Rt
Py3
Ser
20μm
WD = 8.4 mm
Mag = 715 X
Signal A = AsB
SKLaBIG

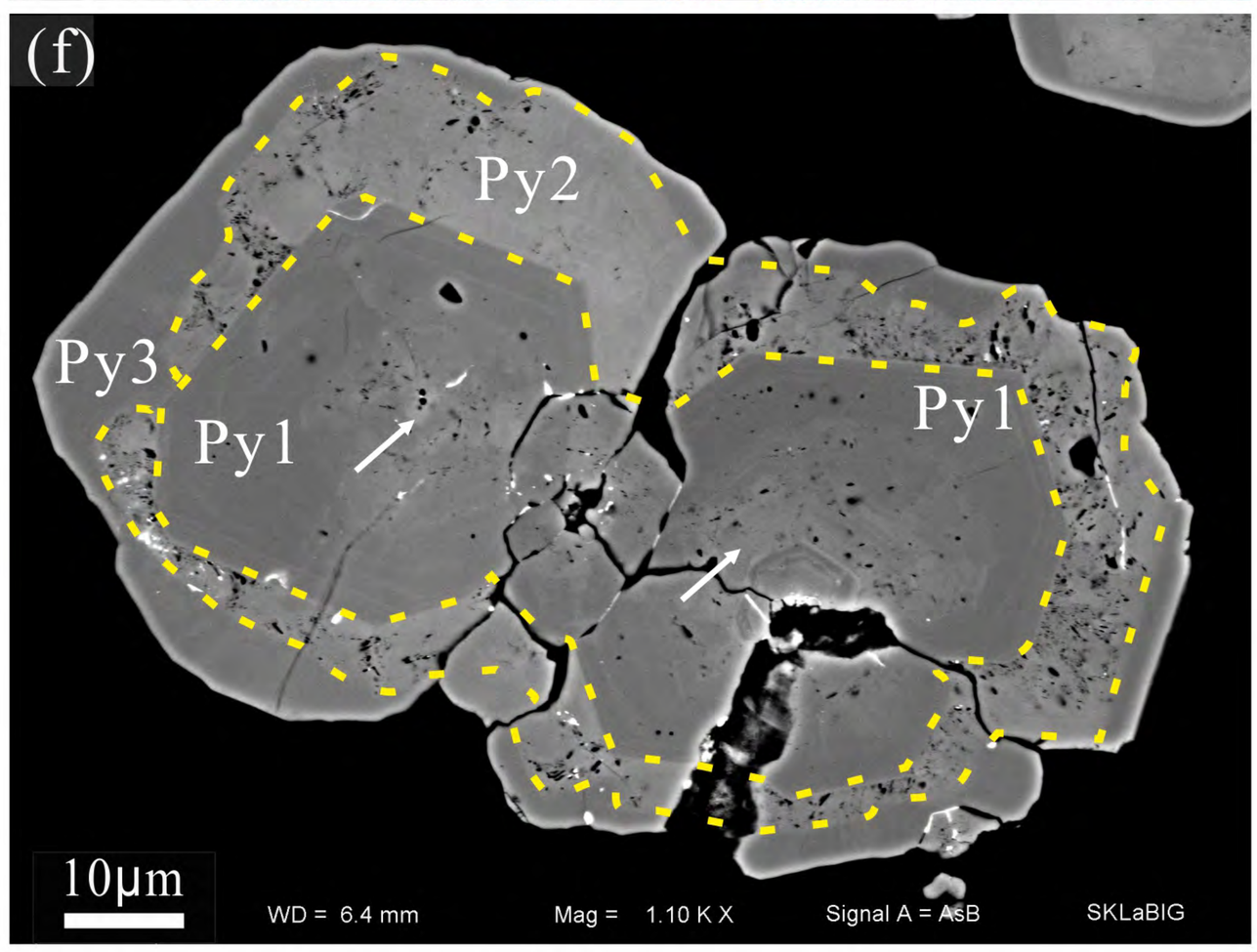
(f)
Py2
Py3
Py1
Py1
10μm
WD = 6.4 mm
Mag = 1.10 K X
Signal A = AsB
SKLaBIG

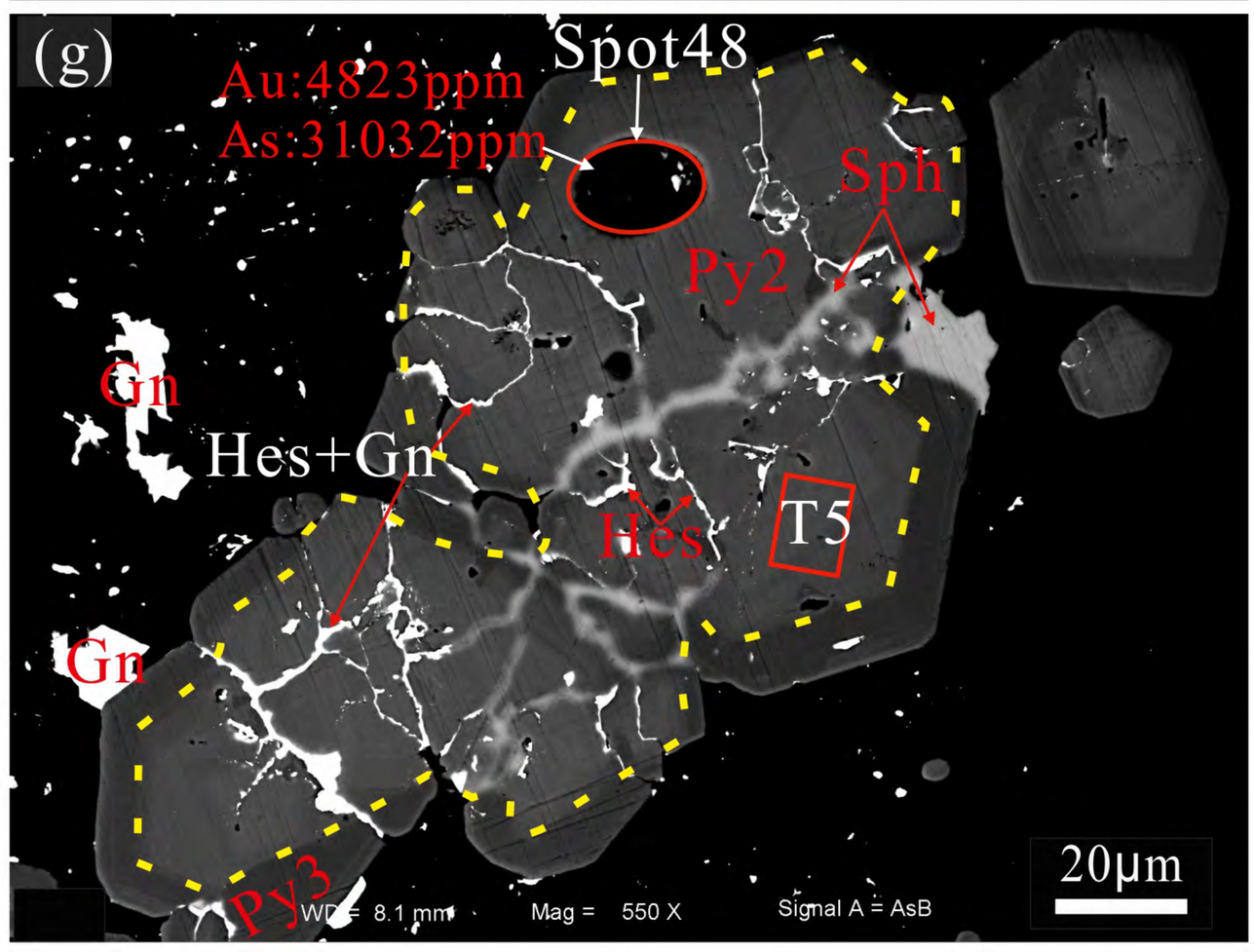
(g)
Au:4823ppm
As:31032ppm
Spot48
Sph
Py2
Gn
Hes+Gn
Hes
T5
Gn
Py3
WD = 8.1 mm
Mag = 550 X
Signal A = AsB
20μm

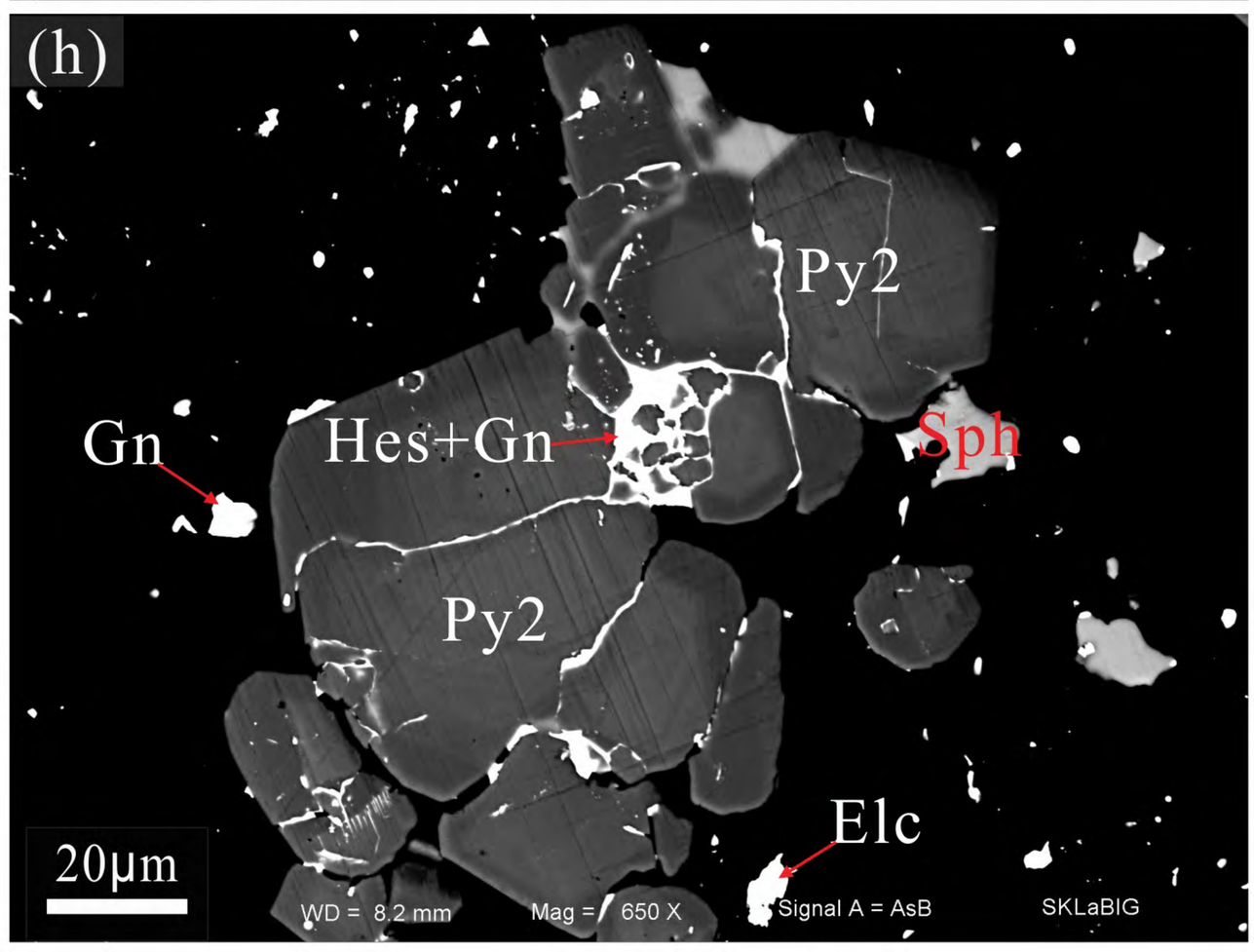
(h)
Py2
Gn
Hes+Gn
Sph
Py2
Elc
20μm
WD = 8.2 mm
Mag = 650 X
Signal A = AsB
SKLaBIG

Fig. 3

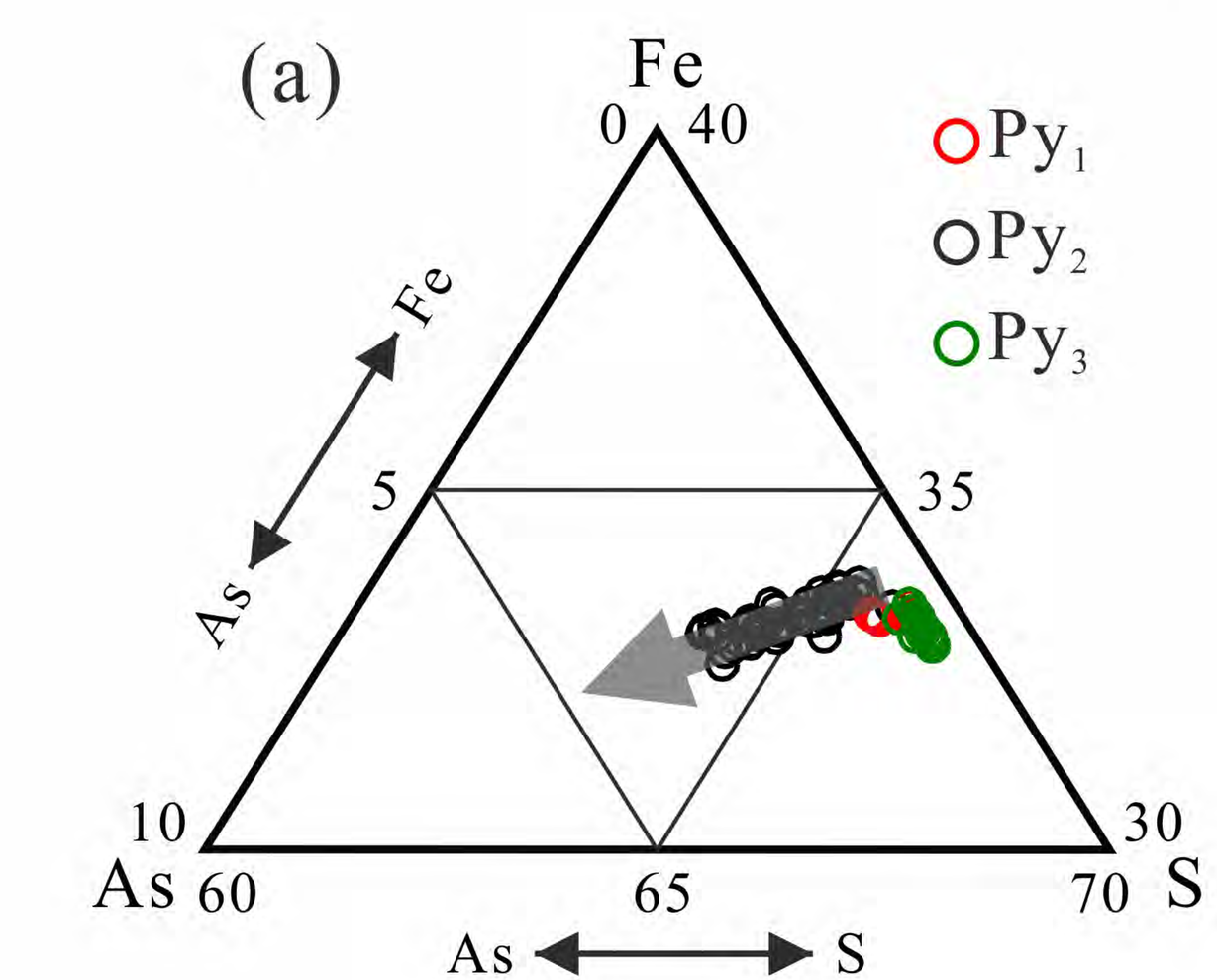
(a)
Fe
0
40
Py1
Py2
Py3
Fe
As
5
35
10
30
As
60
65
70
S
As
S

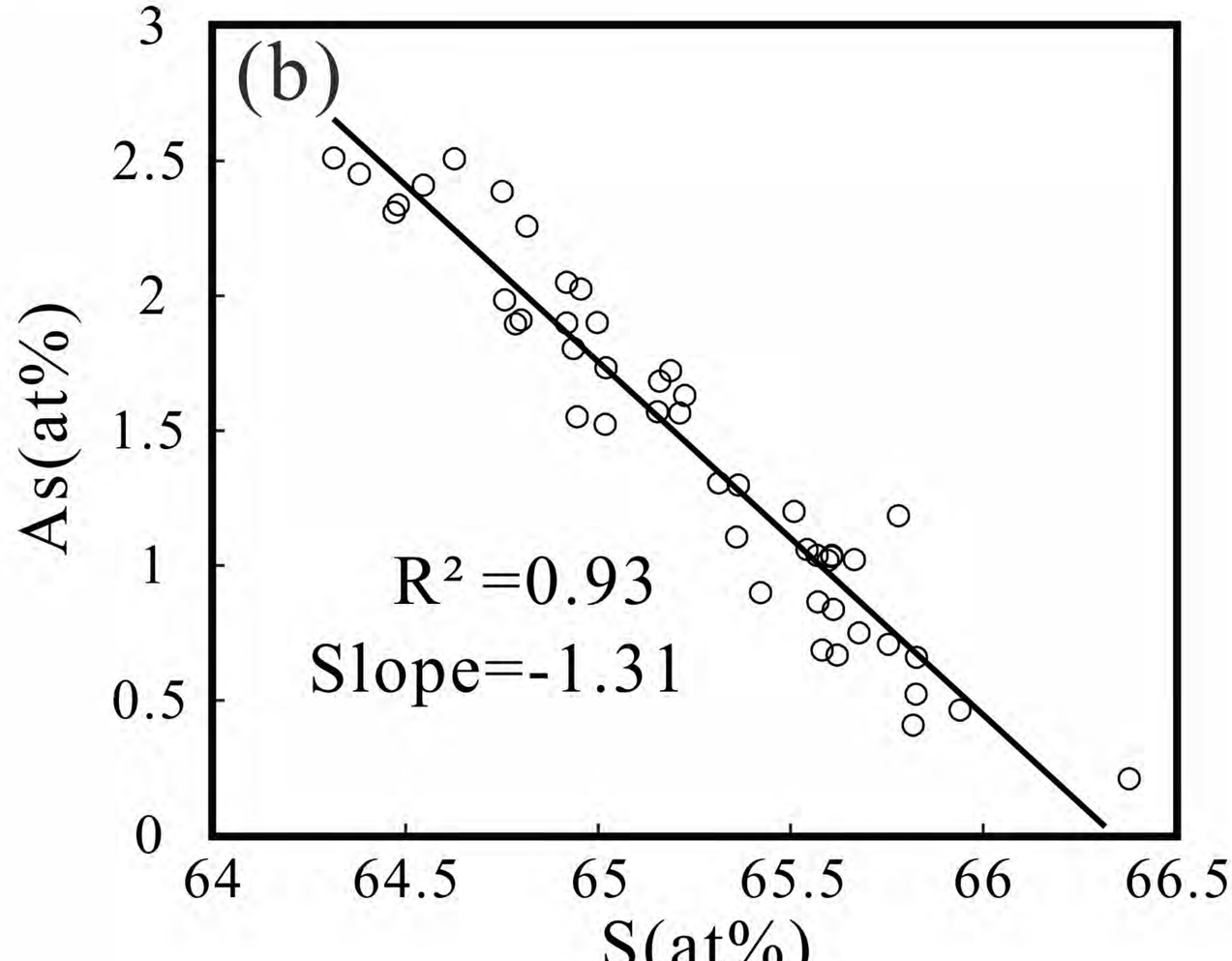
(b)
As(at%)
R² =0.93
Slope=-1.31
S(at%)

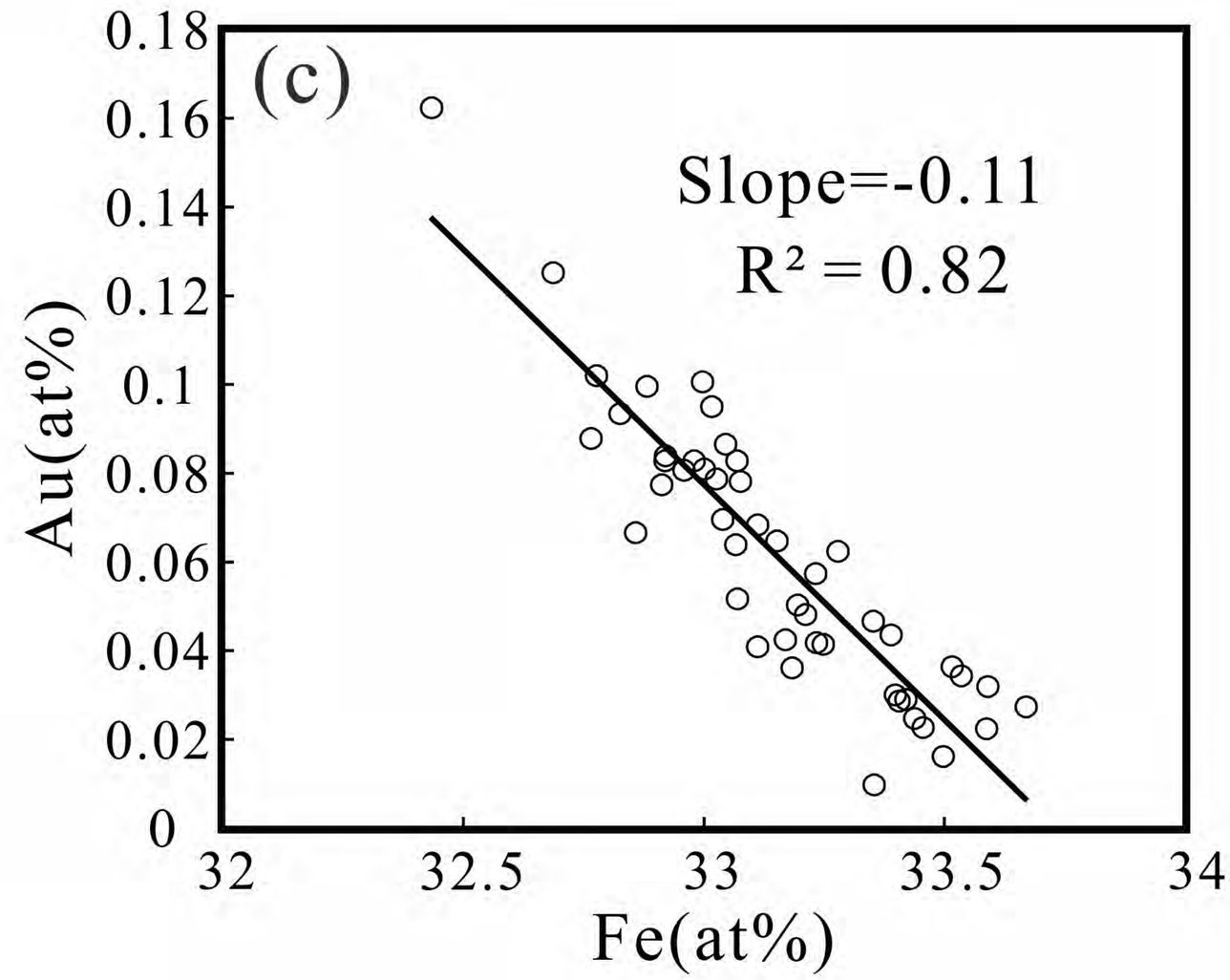
(c)
Slope=-0.11
R² = 0.82
Au(at%)
Fe(at%)

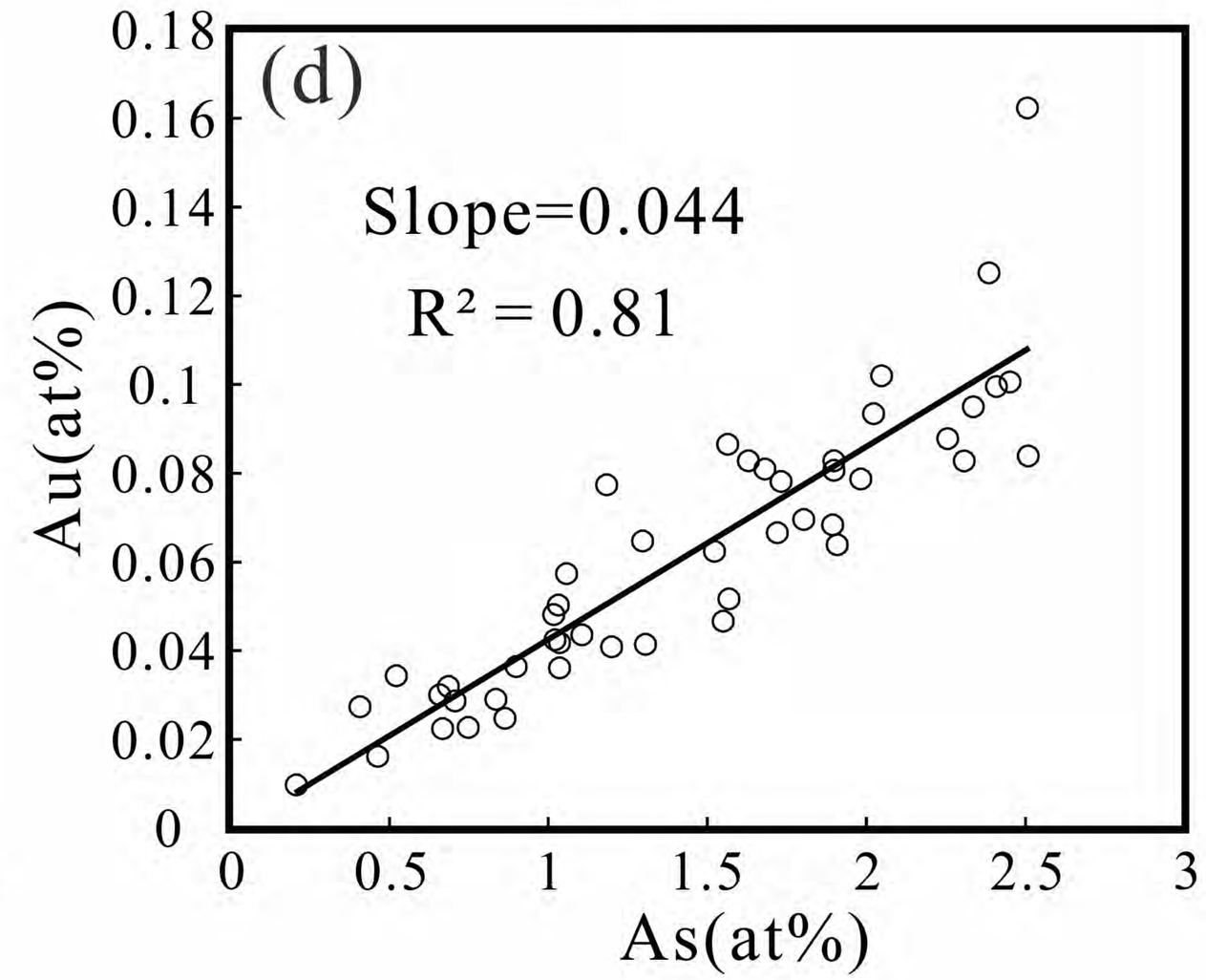
(d)
Slope=0.044
R² = 0.81
Au(at%)
As(at%)

Fig. 4

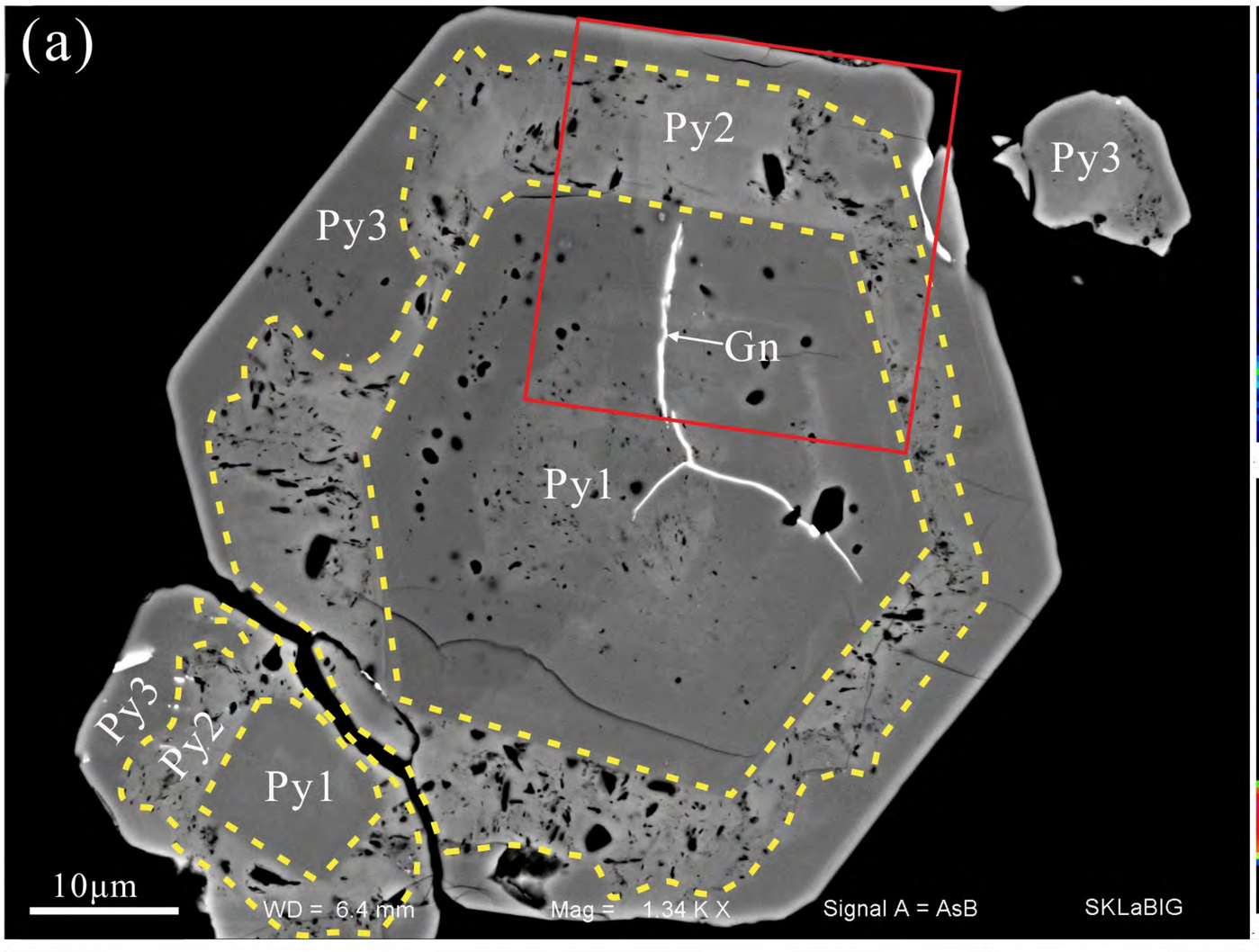

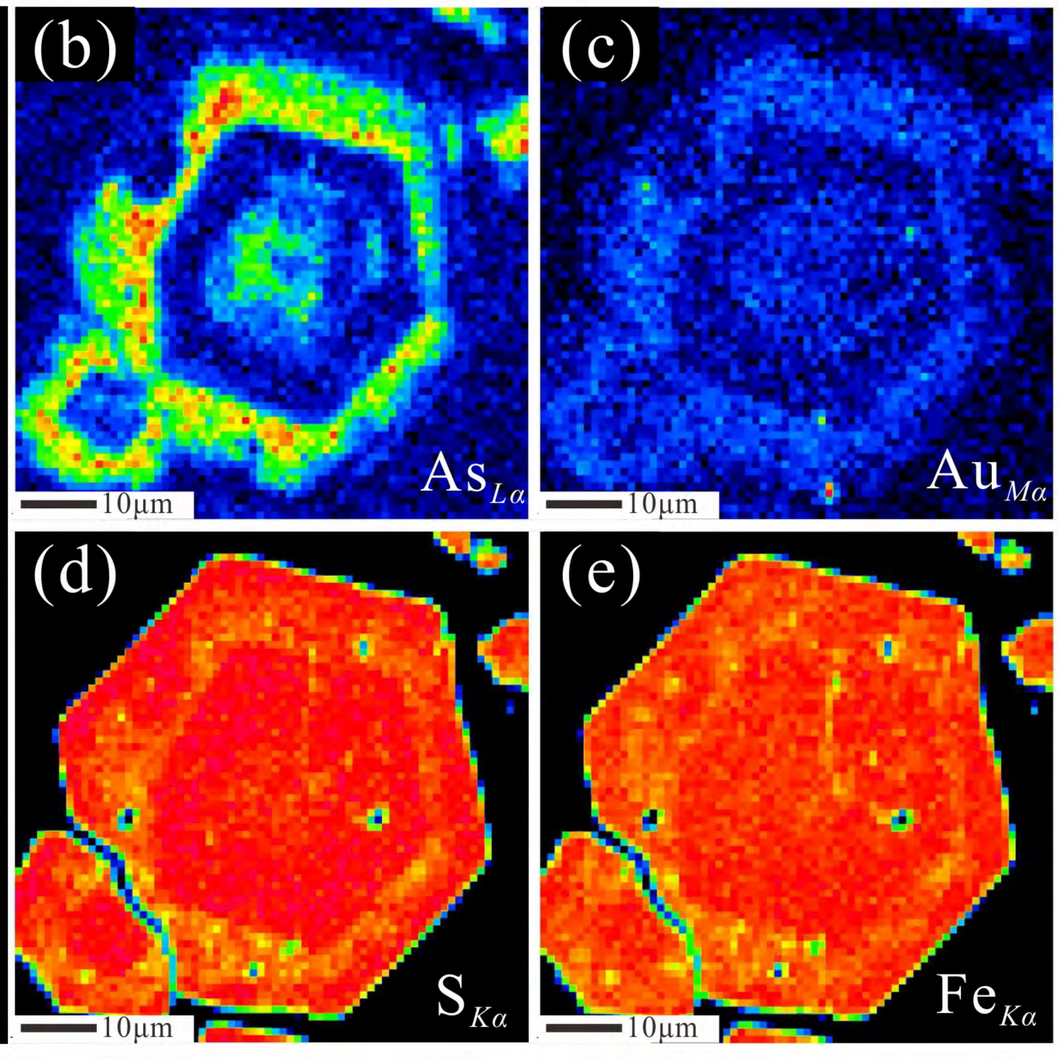

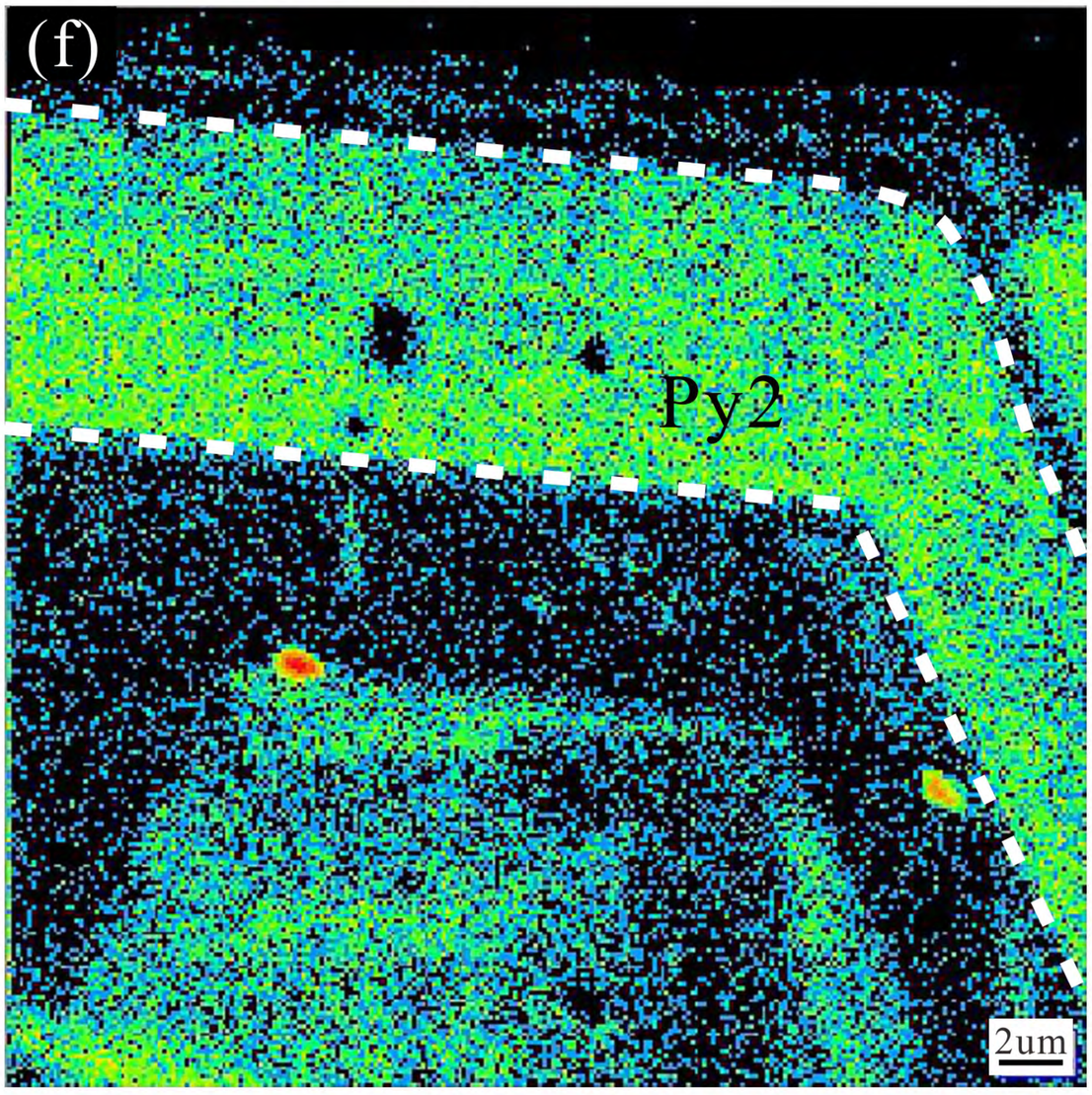

NanoSIMS Mapping 75As32S

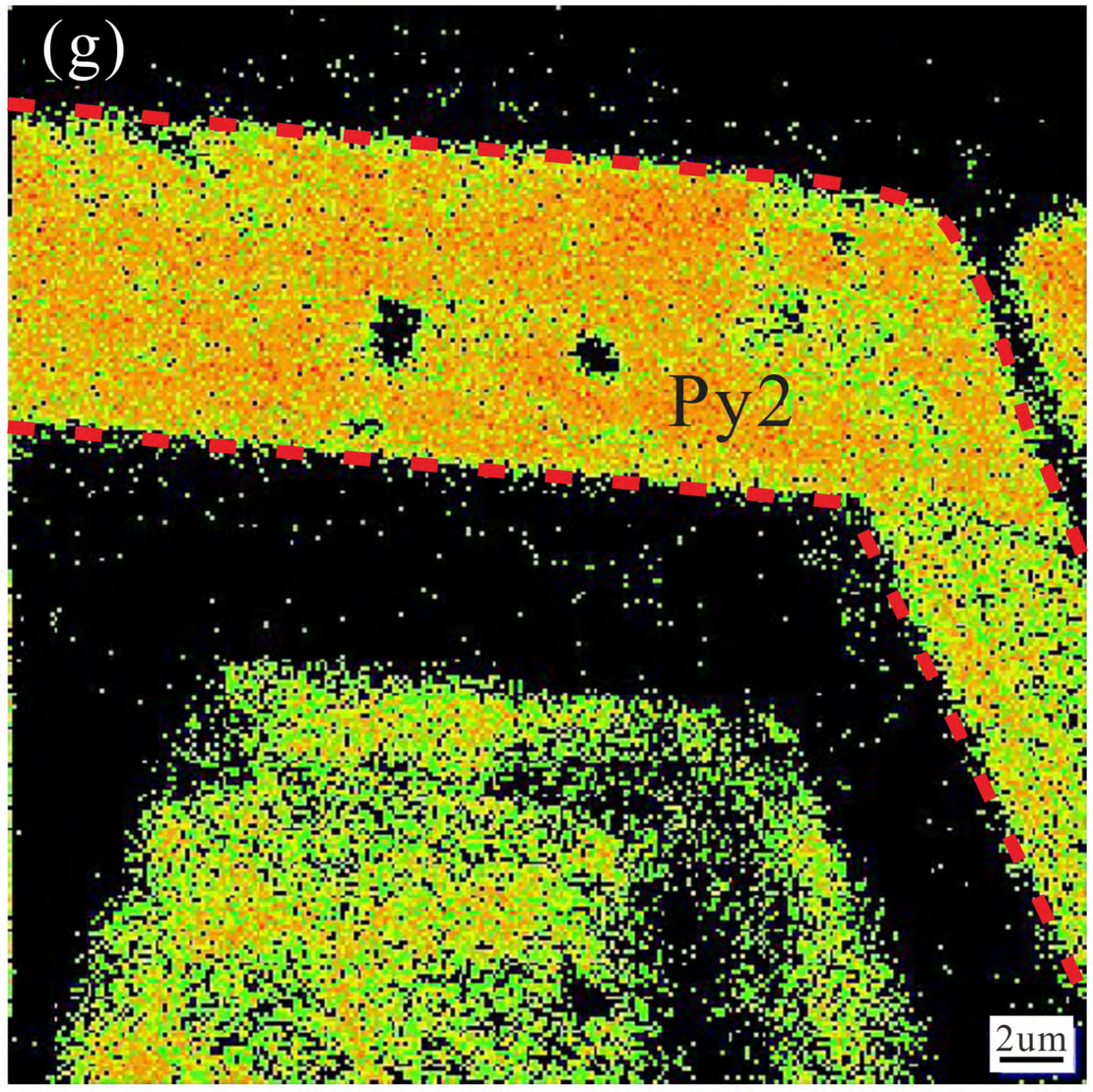

NanoSIMS Mapping 197Au

Fig.5

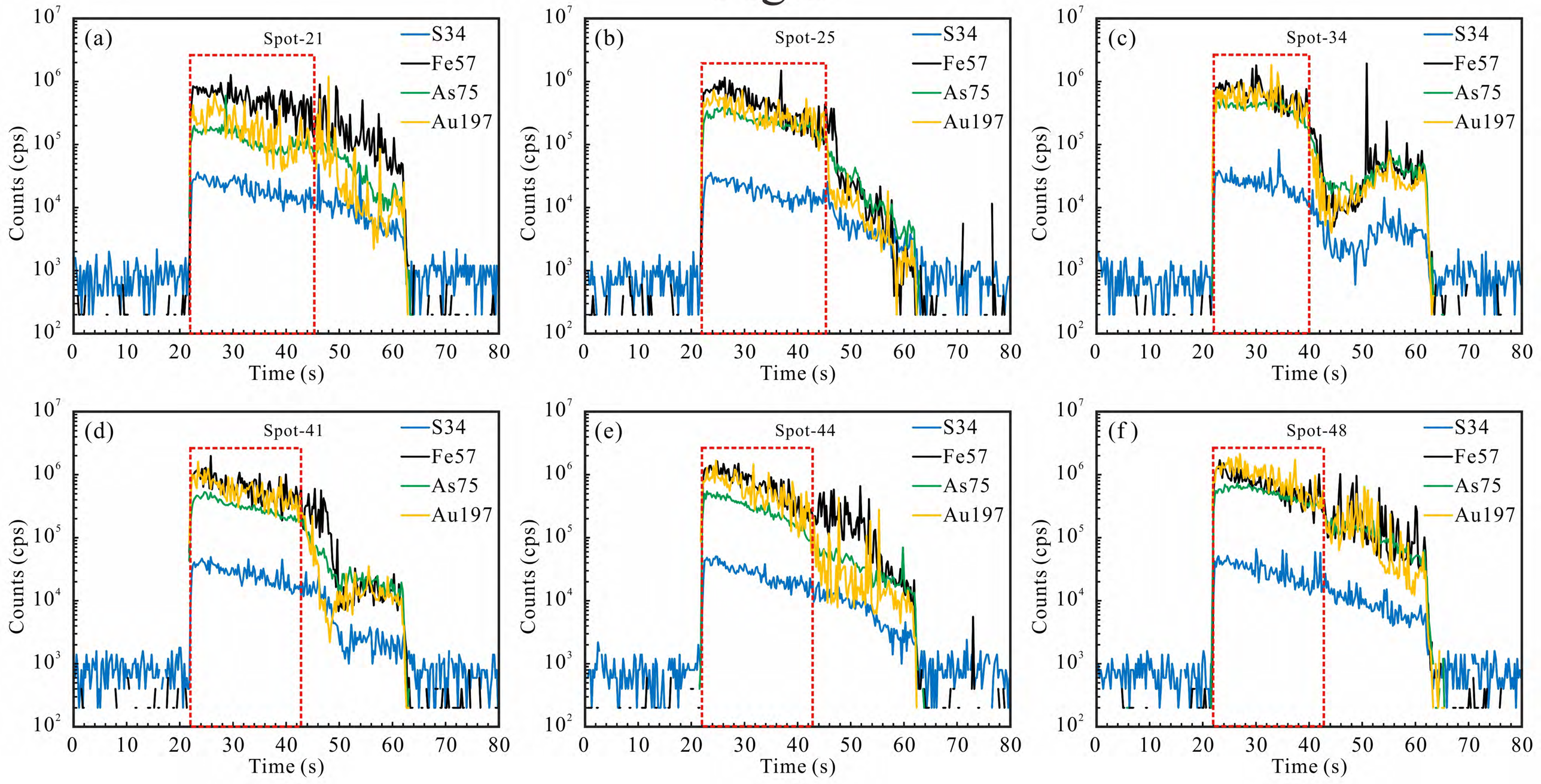
(a)
Spot-21
(b)
Spot-25
(c)
Spot-34
(d)
Spot-41
(e)
Spot-44
(f)
Spot-48
S34
Fe57
As75
Au197
Counts (cps)
Time (s)

Fig. 6

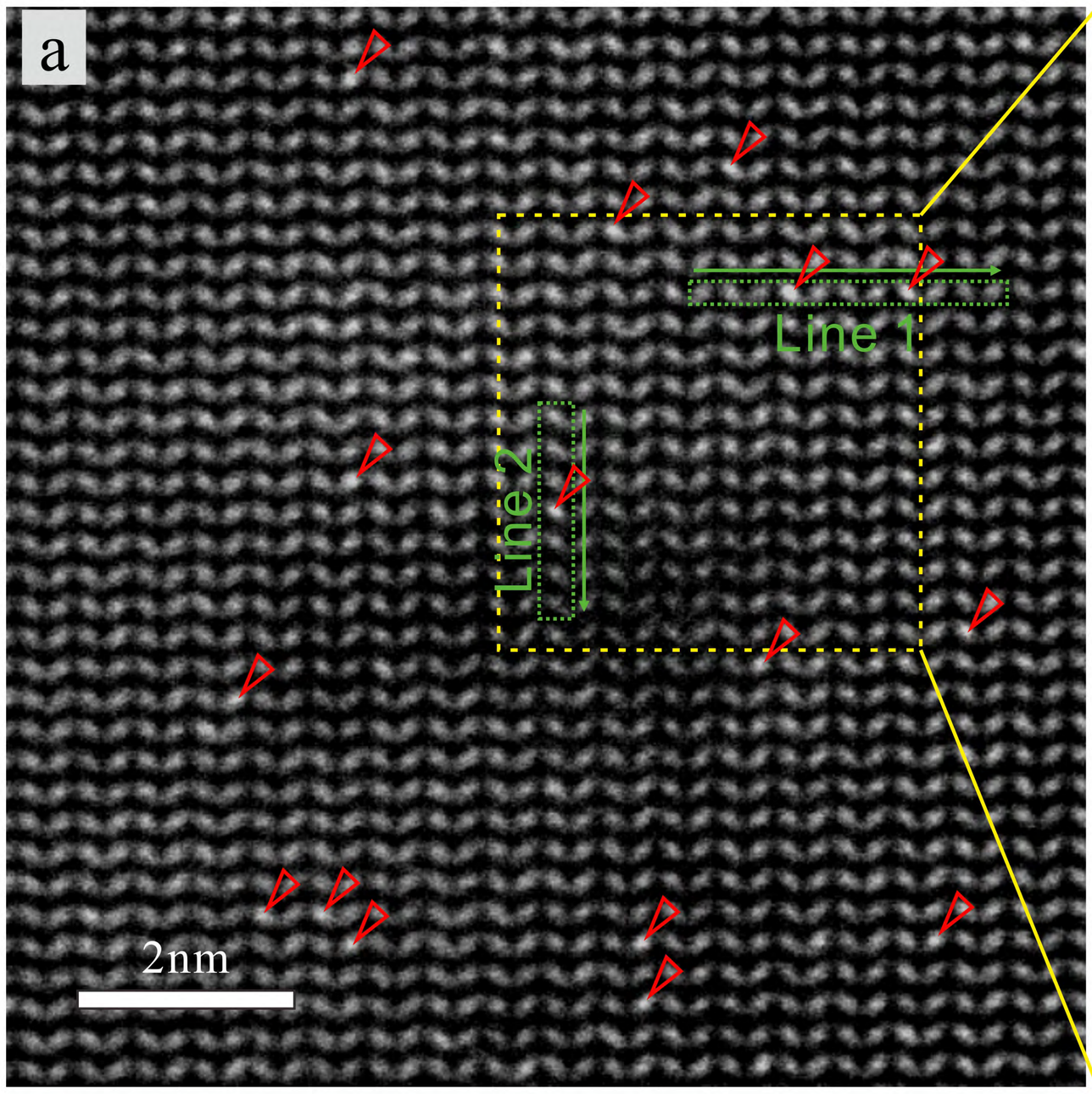
a
Line 1
Line 2
2nm

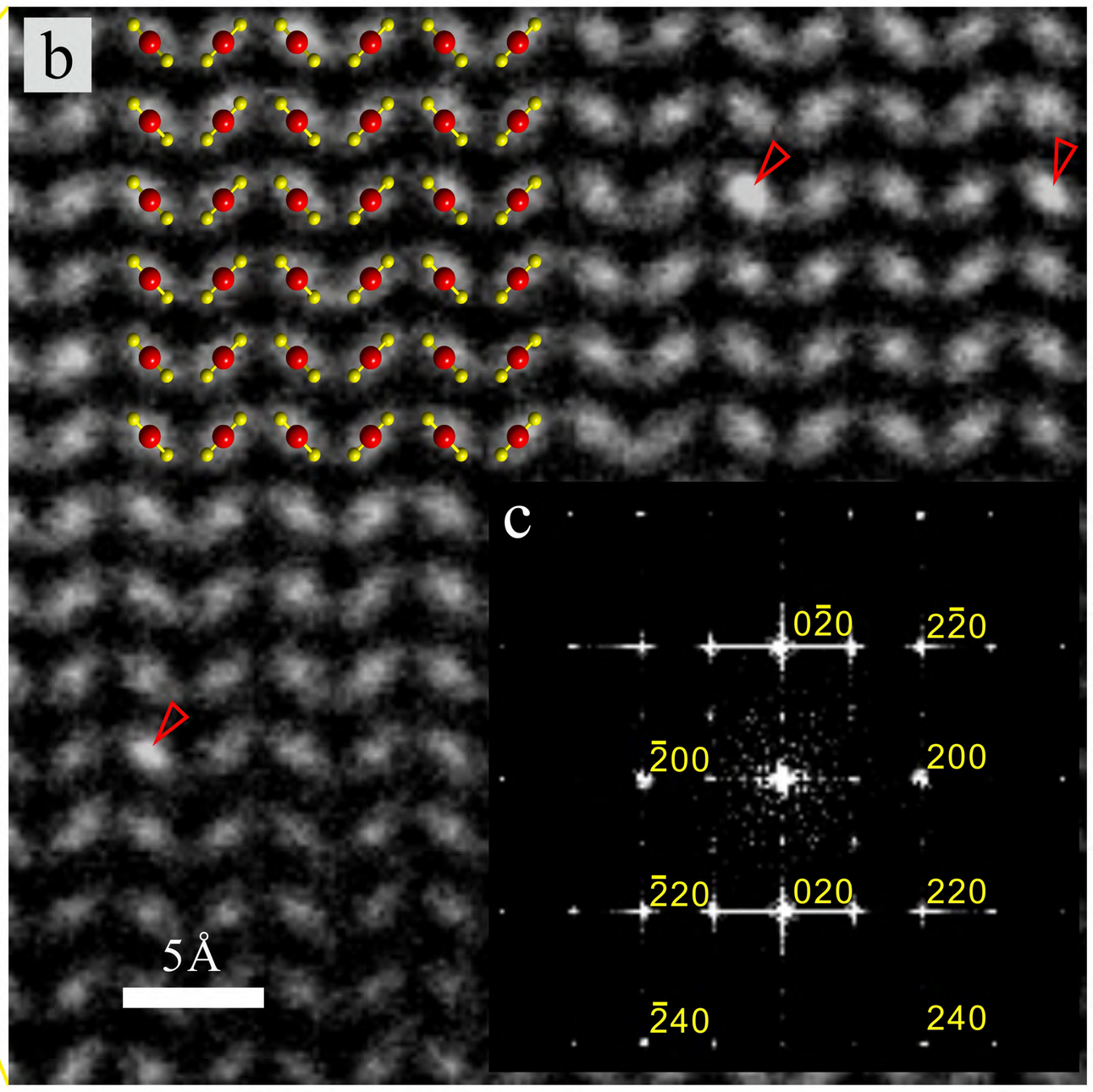
b
5Å
c
0$\bar{2}$0
2$\bar{2}$0
$\bar{2}$00
200
$\bar{2}$20
020
220
$\bar{2}$40
240

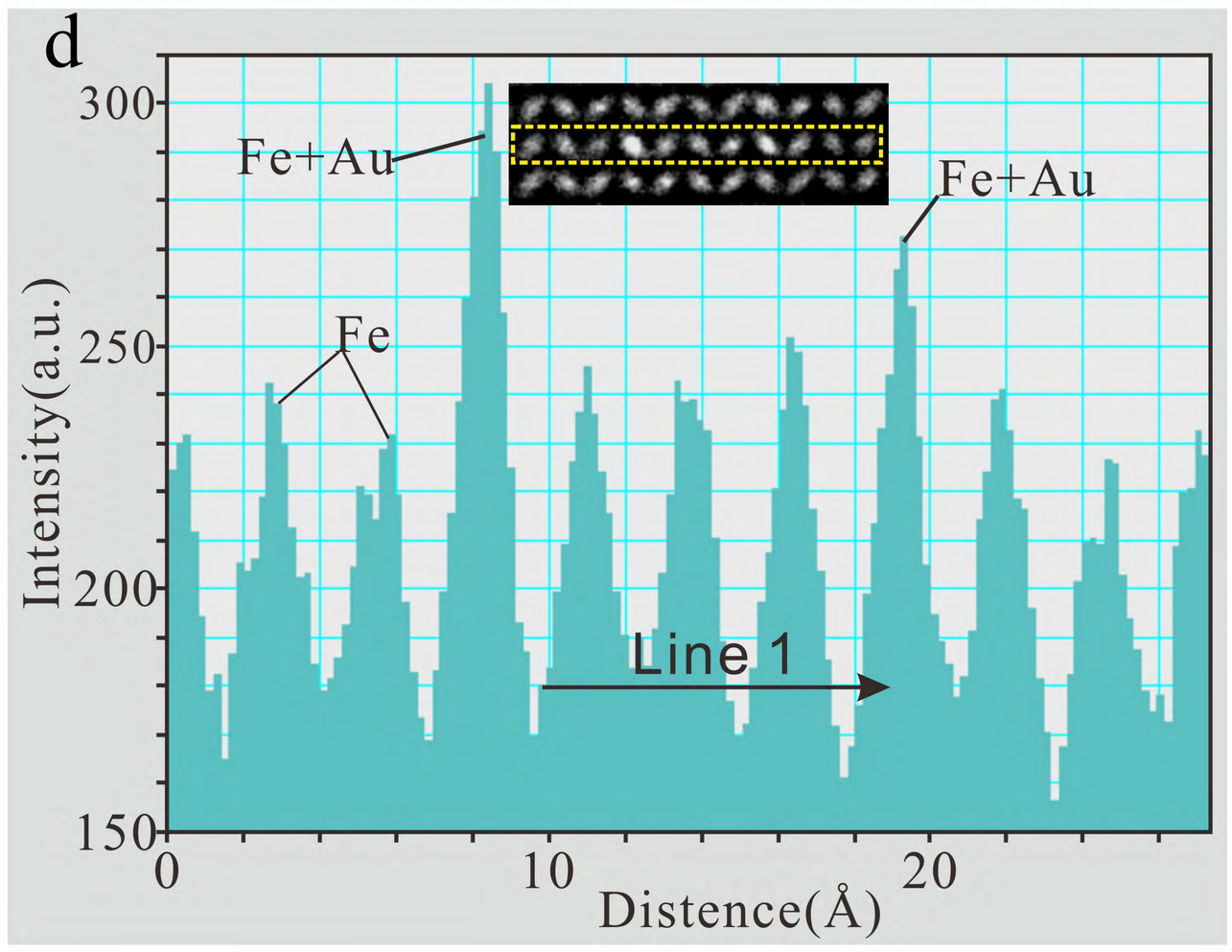
d
Fe+Au
Fe+Au
Fe
Line 1
Intensity(a.u.)
Distence(Å)

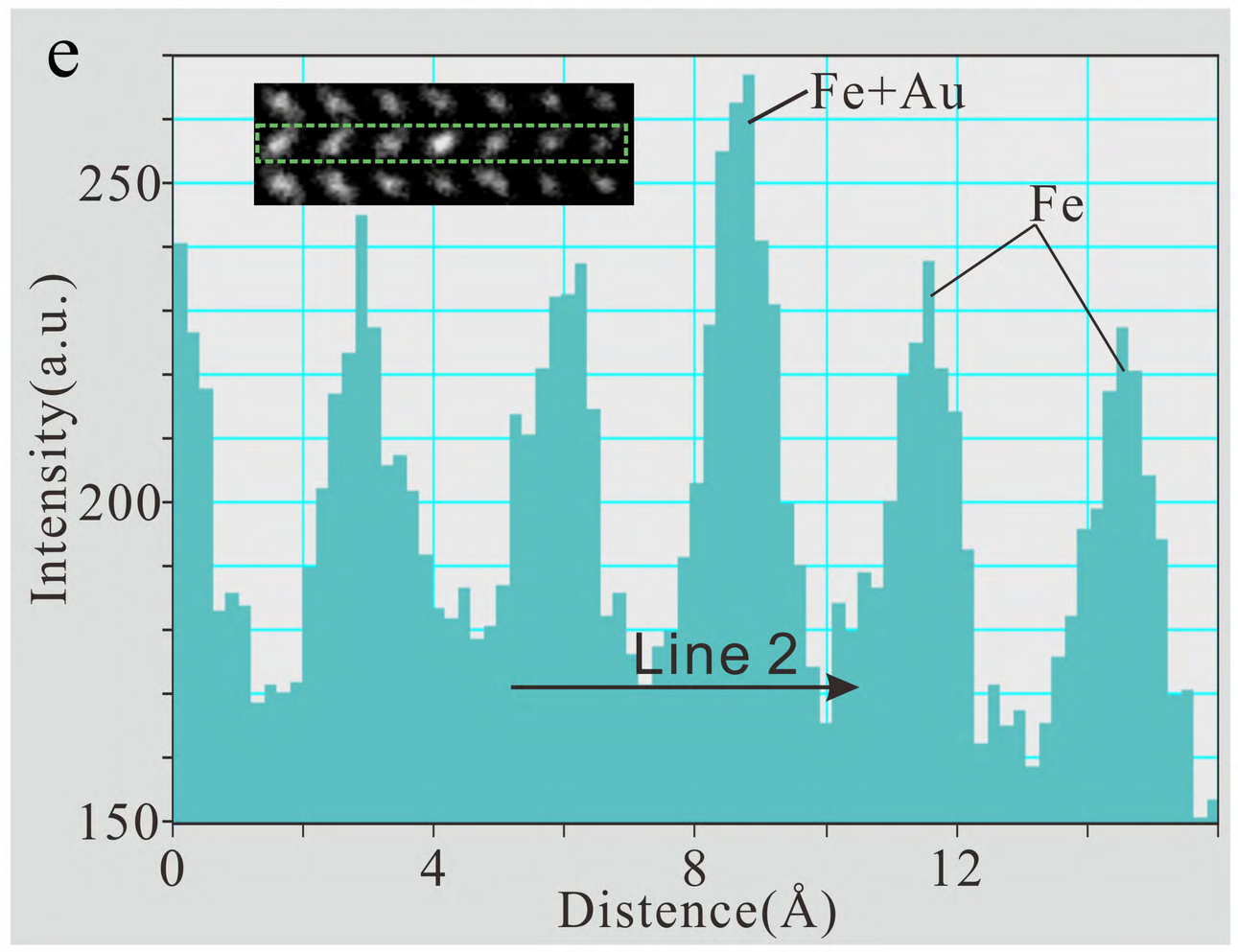
e
Fe+Au
Fe
Line 2
Intensity(a.u.)
Distence(Å)

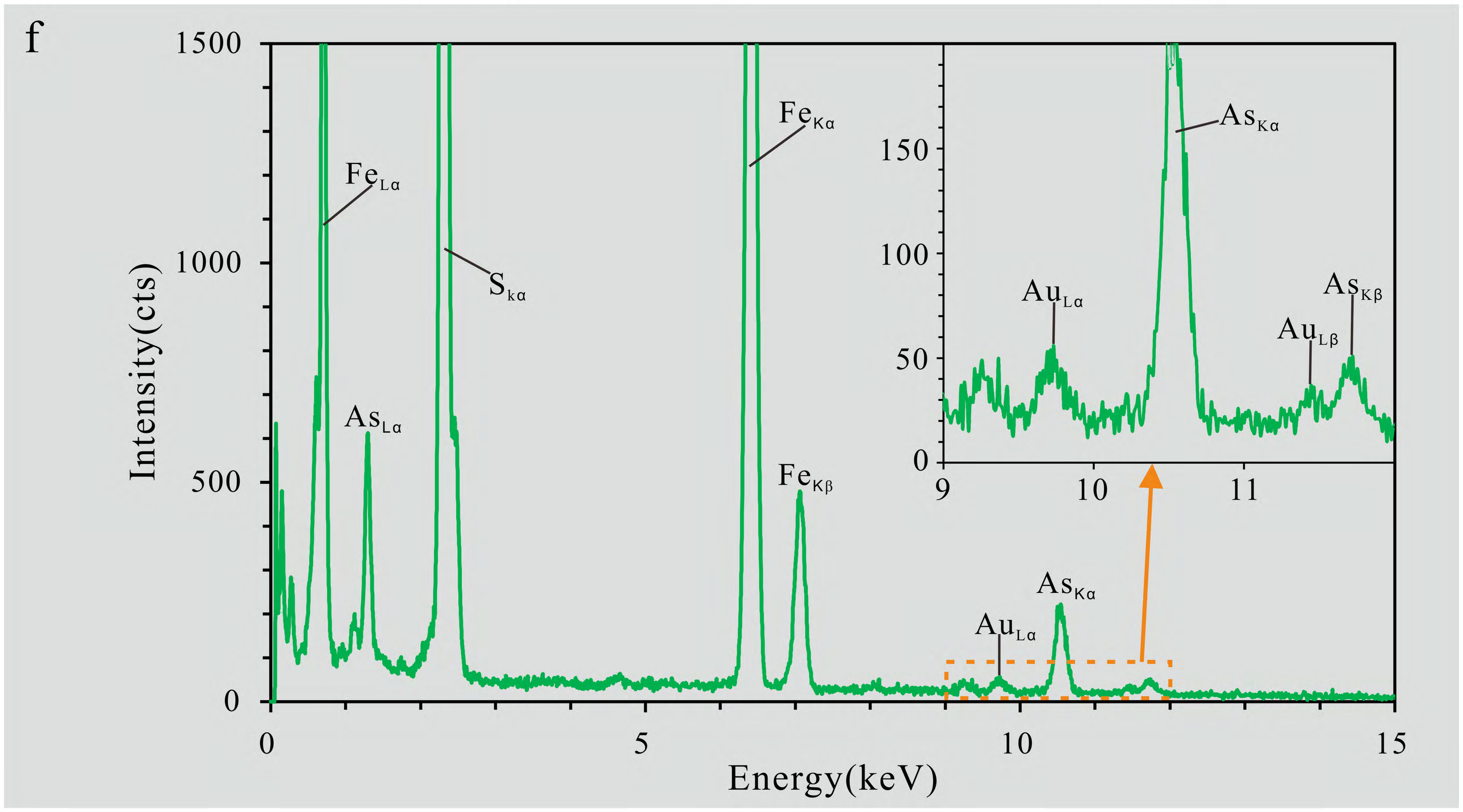
f
$Fe_{L\alpha}$
$S_{k\alpha}$
$As_{L\alpha}$
$Fe_{K\alpha}$
$Fe_{K\beta}$
$As_{K\alpha}$
$Au_{L\alpha}$
$Au_{L\beta}$
$As_{K\beta}$
Intensity(cts)
Energy(keV)

Fig. 7

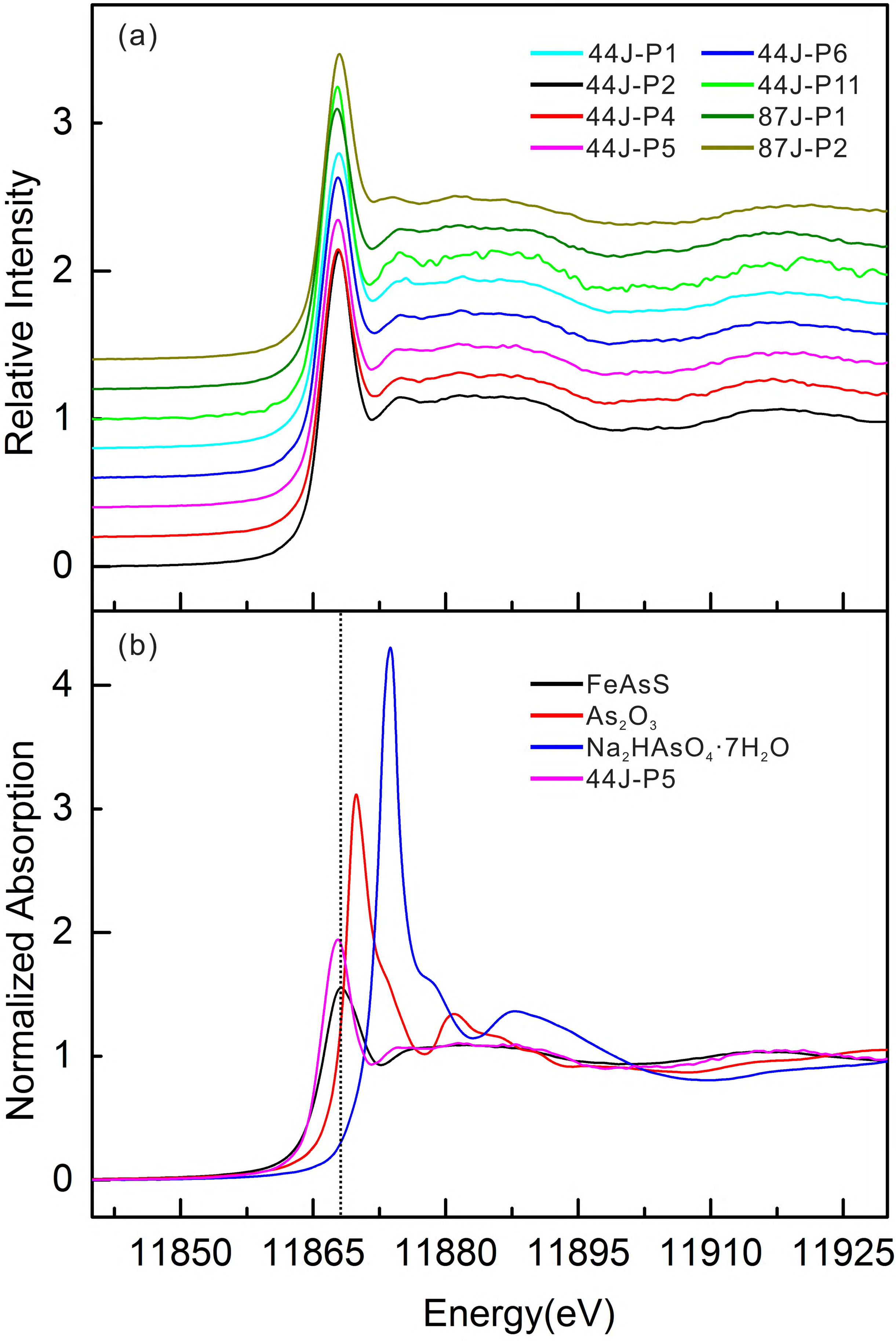
(a)
44J-P1
44J-P2
44J-P4
44J-P5
44J-P6
44J-P11
87J-P1
87J-P2
Relative Intensity
0
1
2
3
(b)
FeAsS
As2O3
Na2HAsO4·7H2O
44J-P5
Normalized Absorption
0
1
2
3
4
11850
11865
11880
11895
11910
11925
Energy(eV)

Fig. 8

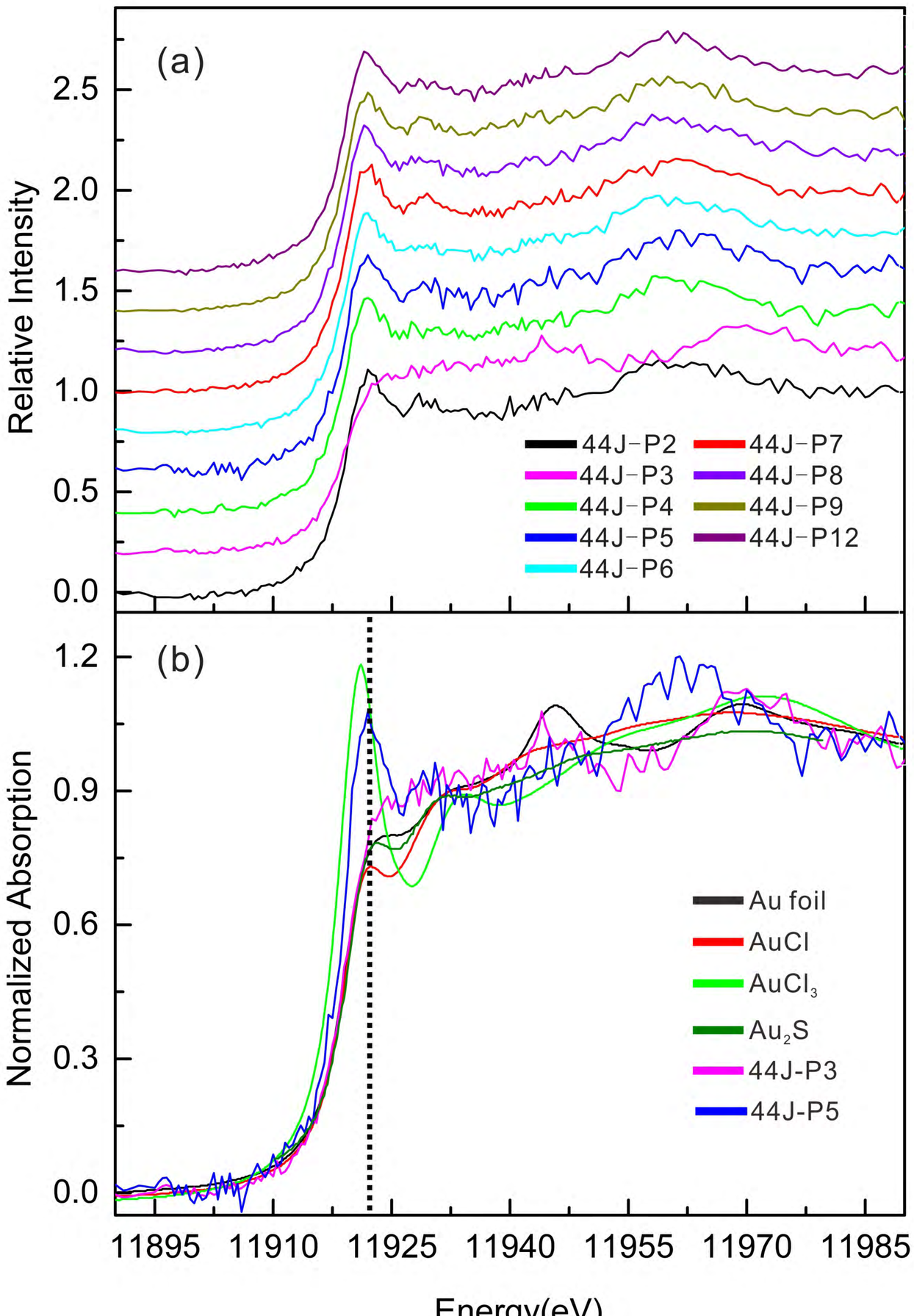
(a)
Relative Intensity
2.5
2.0
1.5
1.0
0.5
0.0
44J-P2
44J-P3
44J-P4
44J-P5
44J-P6
44J-P7
44J-P8
44J-P9
44J-P12
(b)
Normalized Absorption
1.2
0.9
0.6
0.3
0.0
Au foil
AuCl
AuCl3
Au2S
44J-P3
44J-P5
11895
11910
11925
11940
11955
11970
11985
Energy(eV)

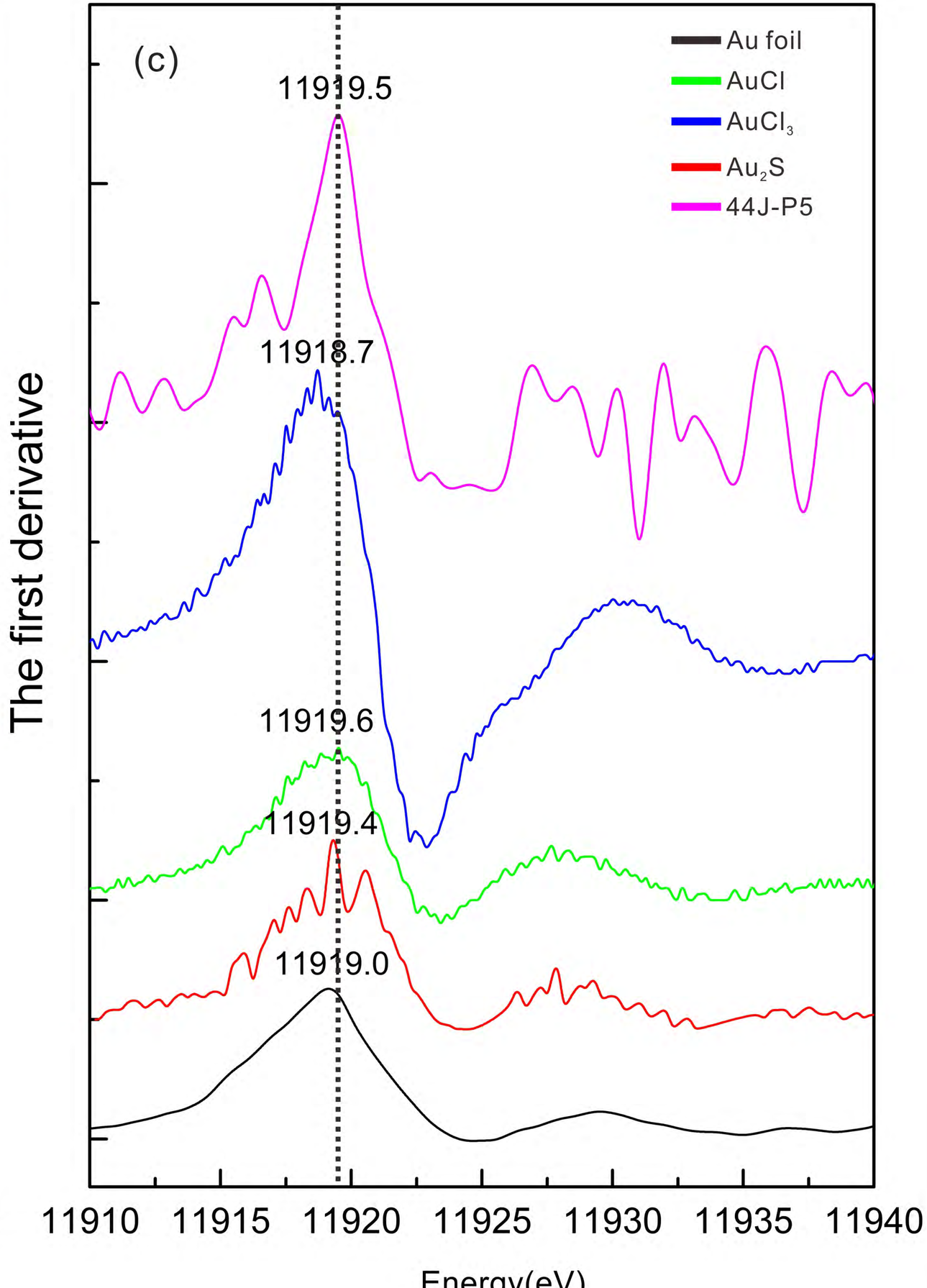
(c)
11919.5
11918.7
11919.6
11919.4
11919.0
Au foil
AuCl
AuCl3
Au2S
44J-P5
The first derivative
11910
11915
11920
11925
11930
11935
11940
Energy(eV)